CHEMISTRY OF MATERIALS

pubs.acs.org/cm

Article

On the Active Components in Crystalline Li–Nb–O and Li–Ta–O Coatings from First Principles

Hengning Chen, Zeyu Deng, Yuheng Li, and Pieremanuele Canepa*

Cite This: https://doi.org/10.1021/acs.chemmater.3c01197

Read Online

ACCESS | Metrics & More | Article Recommendations | Supporting Information

ABSTRACT: Layered-oxide $LiNi_xMn_yCo_{1-x-y}O_2$ (NMC) positive electrodes with high nickel content deliver high voltages and energy densities. However, a high nickel content, e.g., x = 0.8 (NMC811), can lead to high surface reactivity, which can trigger thermal runaway and gas generation. While claimed safer, all-solid-state batteries still suffer from high interfacial resistance. Here, we investigate niobate and tantalate coating materials, which can mitigate the interfacial reactivities in Li-ion and all-solid-state batteries. First-principles calculations reveal the multiphasic nature of Li–Nb–O and Li–Ta–O coatings, containing mixtures of $LiNbO_3$ and Li_3NbO_4 or of $LiTaO_3$ and Li_3TaO_4. The concurrence of several phases in Li–Nb–O or Li–Ta–O modulates the type of stable native defects in these coatings. Li–Nb–O and Li–Ta–O coating materials can favorably form lithium vacancies Vac'_{Li} and antisite defects $Nb^{\bullet\bullet\bullet\bullet}_{Li}$ ($Ta^{\bullet\bullet\bullet\bullet}_{Li}$) combined into charge-neutral defect complexes. Even in defective crystalline $LiNbO_3$ (or $LiTaO_3$), we reveal poor Li-ion conduction properties. In contrast, Li_3NbO_4 and Li_3TaO_4 that are introduced by high-temperature calcinations can provide adequate Li-ion transport in these coatings. Our in-depth investigation of the structure–property relationships in the important Li–Nb–O and Li–Ta–O coating materials helps to develop more suitable calcination protocols to maximize the functional properties of these niobates and tantalates.

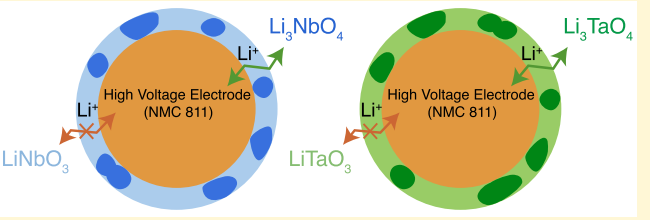

1. INTRODUCTION

Notwithstanding the maturity of the lithium (Li)-ion battery technology, stabilizing the electrode–electrolyte interfaces and interphases sets challenges in lithium-ion batteries (LIBs), as well as in novel all-solid-state batteries (ASSBs).[1,2] For example, in LIBs, hydrofluoric acid released upon $LiPF_6$ decomposition can lead to the surface corrosion of cathode particles and subsequent leaching of transition-metal ions (TMs) into the electrolyte.[2] Furthermore, during reversible Li intercalation in cathode active materials (CAMs), significant volume variations of the active particles may induce cracks that lead to loss of contact among the active particles, and a subsequent reduction in performance.[3]

Thiophosphate solid electrolytes (SEs), e.g., $Li_{10}GeP_2S_{12}$ (LGPS) and argyrodites Li_6PS_5X (with X = Cl, Br, I),[4] display high Li-ion conductivities and low-temperature processability and hence are promising candidates for ASSBs. However, the low oxidative (or anodic) stabilities of thiophosphate SEs can result in undesired side reactions, especially with high-voltage (>4.5 V vs. Li/Li^+) CAMs.[5,6]

Introducing coating materials is one of the most effective solutions to mitigate possible interfacial instabilities in LIBs and ASSBs, improving their capacity retention, rate capabilities, and longevity of cells.[7−9] Coating materials can enhance the "adhesion" between cathode particles and act as physical protections from undesired chemical reactions. Coating materials also stabilize the cathode–electrolyte interfaces chemically and electrochemically, thereby increasing or modulating the stability windows of electrolytes.

Simultaneously, coatings in LIBs are designed to have high ionic and electronic conductivities—both properties are essential for maintaining percolating ionic and electronic networks between cathode particles.[2] The requirements of coatings (for cathode electrodes) in ASSBs are different from LIBs: (i) deliver high Li-ion conductivity, and (ii) maintain sufficiently low electronic conductivity to prevent SEs with narrow stability windows from being easily oxidized by high-voltage CAMs.[9]

In particular, amorphous $LiNbO_3$ and $LiTaO_3$ materials with high ionic conductivities ($\sim 10^{-5}$–10^{-6} S cm^{-1} at room temperature) and appreciable electronic resistance ($\sim 10^{-11}$–10^{-12} Ω^{-1} cm^{-1}) have been effectively used as coatings in ASSBs.[10−12] Albeit with much lower Li-ion conductivities ($<10^{-12}$ S cm^{-1} at 400 K) and exceedingly high migration barriers (1.16–1.33 eV),[13,14] crystalline $LiNbO_3$ and $LiTaO_3$ coatings show substantial enhancements in the electrochemical performance of LIBs (see Table S1).[15−18]

Received: May 19, 2023
Revised: June 21, 2023

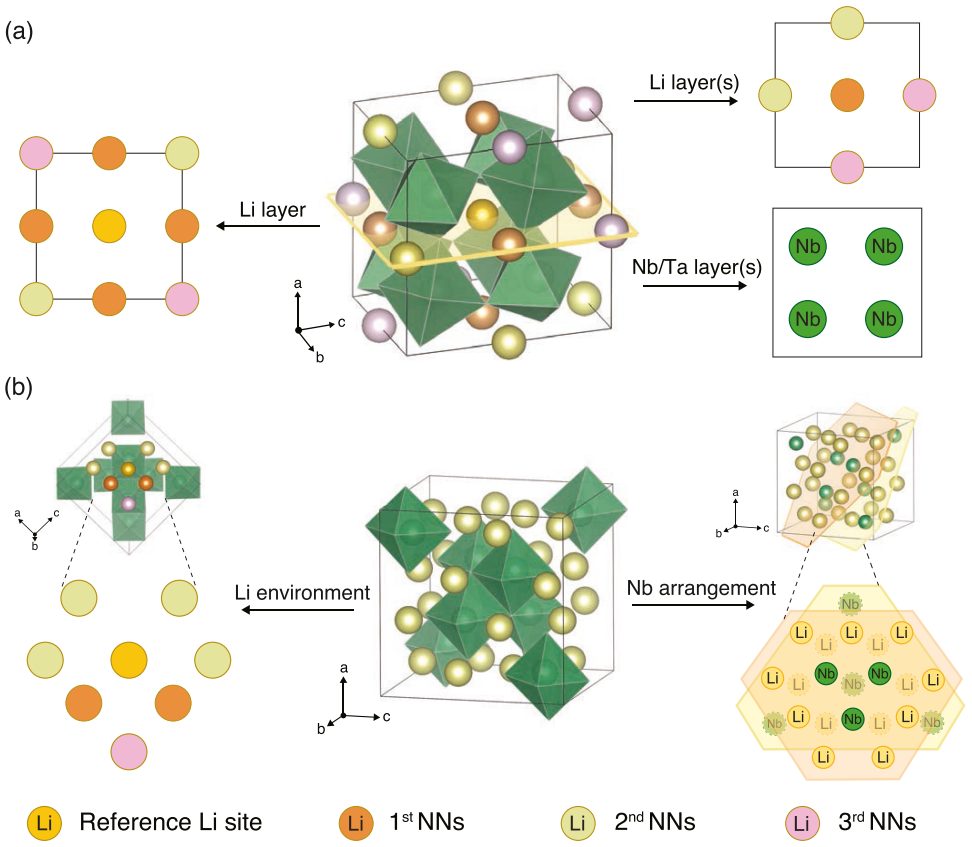

Figure 1. (a) Structures of $LiNbO_3$ ($LiTaO_3$) ($R3c$) with corner-sharing Nb(Ta)O_6 octahedra, transformed into pseudo-cubic structures using the [[1, 1, −1], [−1, 1, 1], [1, −1, 1]] transformation matrix. (b) Structure of Li_3NbO_4 ($I\bar{4}3m$) with edge-sharing Nb(Ta)O_6 octahedra. For the centered Li site in $LiNbO_3$ ($LiTaO_3$) in panel (a), there are two first nearest neighbors (NNs), four second NNs, four third NNs at the top and bottom Li layers, and four first NNs, two second NNs, two third NNs on the middle Li layer, as well as eight nearby Nb(Ta) atoms. The left panel in (b) describes the local environment of a Li site in Li_3NbO_4, and the right panel shows the arrangement of four Nb atoms within Nb_4O_{16} clusters at the center of orange and yellow planes. Additional views of these structures emphasizing the Li-ion environments are presented in Figure S2.

As the information available in the literature on amorphous and crystalline phases of niobate and tantalate coatings appears scattered, it is important to set a firm baseline on the crystalline phases of these materials. While amorphous niobates and tantalates appear to provide the highest ionic conductivities,[10,13,19] the crystalline analogues are reported to increase the hardness of cathode particles.[20,21]

Although higher levels of crystallinity in $LiNbO_3$ (or $LiTaO_3$) have been linked to a reduction of CAM particle cracking,[20,21] there exists an apparent contradiction between the low Li-ion conductivity of crystalline $LiNbO_3$ (or $LiTaO_3$) and the good rate capabilities achieved in these cells.[15,19] Indeed, the texture and composition of these niobate and tantalate materials appear evidently more complicated than commonly perceived.

Previous reports[13,14] suggested that highly defective nanocrystalline $LiNbO_3$ and $LiTaO_3$ (from high-energy ball milling) containing amorphous-like components exhibit room-temperature Li-ion conductivities ($\sim 10^{-6}$ S cm^{-1}), comparable with their amorphous analogues (10^{-5}–10^{-6} S cm^{-1}). These facts hint at the high sensitivity of Li-ion conductivity in $LiNbO_3$ and $LiTaO_3$ to the presence of defects in their crystalline phases.

Conventional synthesis protocols of crystalline niobate (or tantalate) coatings typically apply the wet-chemical method followed by prolonged (3–10 h long) calcinations at 773–1073 K (Table S1). Furthermore, $LiMO_3$ (with M = Nb and Ta) tends to crystallize out from the congruent melts (Li-poor, M-rich) at off-stoichiometric compositions, facilitating the incorporation of intrinsic defects (see Figure 3).[22−25] However, neutron reflectometry and secondary ion mass spectroscopy measurements did not suggest a marked increase in Li-ion transport in these materials.[26,27] Therefore, the role played by intrinsic defects in the functional properties of niobate and tantalate coatings remains ambiguous.

Recent investigations on the composition of Li−Nb−O coating highlight the coexistence of two primary phases: $LiNbO_3$ and Li_3NbO_4.[15,16,28] Zhang et al.[15] suggested that the coexistence of $LiNbO_3$ and Li_3NbO_4 improves the electrochemical performances of coated cathodes. Several reports suggested that the Li^+ migration barrier in crystalline Li_3NbO_4 (0.58–0.85 eV) is considerably lower than that of crystalline $LiNbO_3$ (1.16–1.33 eV).[19,29] Liao et al. and Yabuuchi et al. showed an increase in Li-ion conductivity by several orders of magnitude in Li_3NbO_4 upon doping with W^{6+}, or substituting of Ni^{2+} for Li^+, which introduces Li vacancies.[29,30] This evidence suggests Li_3NbO_4 may be the active phase in transporting Li ions in niobate coatings.

Based on the facts exposed above, protocols employed for synthesizing crystalline niobate coatings can strongly affect: (i) the partition of the active phases of Li−Nb−O coatings,[16,28] (ii) the concentrations of intrinsic defects, and in turn affect (iii) the Li-ion diffusion in these materials. This knowledge gap requires immediate attention to optimize the functional properties of niobates and tantalates.

https://doi.org/10.1021/acs.chemmater.3c01197
Chem. Mater. XXXX, XXX, XXX−XXX

Leveraging a combination of first-principles calculations (density functional theory, DFT), bond valence mapping (through the *SoftBV*),[31] nudged elastic band (NEB) calculations, and machine-learning (ML) molecular dynamics (MDs), we investigate how the Li migration properties of $LiMO_3$ and Li_3MO_4 (with M = Nb and Ta) are modulated by the occurrence of thermodynamically viable intrinsic defects. We demonstrate that what is commonly perceived as a $LiNbO_3$ (or $LiTaO_3$) coating material, in practice, is a multiphasic composite including variable fractions of Li_3NbO_4 (or Li_3TaO_4), altering the conduction property of the material. The occurrence of intrinsic defects in niobates (and tantalates) remains conditional to the coexistence of $LiMO_3$ and Li_3MO_4 at synthesis conditions, which regulates the availability of Li vacancies. A progressive transformation of $LiMO_3$ into Li_3MO_4 by prolonged high-temperature calcination results in a much less defective Li_3MO_4 coating material, which in turn hinders Li^+ transport and deteriorates the functionality of the coating.

2. CRYSTAL STRUCTURES OF $LIMO_3$ AND LI_3MO_4

Figure 1 shows $LiNbO_3$ and $LiTaO_3$ perovskite structures (space group *R*3*c*), which present octahedra tilting.[32,33] In $LiNbO_3$ ($LiTaO_3$), surrounded by oxygen atoms, Li and Nb (Ta) cations occupying 2/3 octahedral sites are aligned along the *c*-axis (see Figure S1) and follow a stacking sequence of Nb (Ta), Li (or vacancy), and Nb (Ta).[22] Both $LiNbO_3$ and $LiTaO_3$ show a single Li Wyckoff site.

We analyze the immediate environment of Li ions (gold atom in Figure 1a), which is important to set up different models of intrinsic defect complexes, and investigate Li-ion migration pathways in $LiNbO_3$ and $LiTaO_3$. For a Li site in $LiNbO_3$ and $LiTaO_3$, there are six first nearest neighbors (NNs), six second NNs, and six third NNs Li sites in total from the top, middle, and bottom Li layers, respectively. The eight neighboring $Nb(Ta)O_6$ are shown in Figure 1a as green octahedra.

Li_3NbO_4 shows a disordered rock-salt structure with an average $Fm\bar{3}m$ space group (Figure S3) when synthesized at a low temperature (at ~220 °C).[34,35] At 700 °C, Li_3NbO_4 transforms into an $I\bar{4}3m$ ordered phase (Figure 1b),[36−38] which highlights the edge-sharing NbO_6 octahedra. In the right panel of Figure 1b, three Nb cations (at the center) form a tetramer (Nb_4O_{16}) with the other Nb cation in subsequent layers. Together with Li ions (and vacancies), these Nb_4O_{16} clusters form a body-centered cubic lattice. Compared with the *R*3*c* closely packed $LiNbO_3$, this arrangement might allow larger voids that facilitate Li transport. For each Li site, there are two first NNs, four second NNs, and one third NN as shown in the left panel of Figure 1b.

Li_3TaO_4 exists in three main polymorphs (Table S3): (i) a disordered low-temperature phase with an average space group $Fm\bar{3}m$ (similar to Li_3NbO_4, Figure S3), (ii) an intermediate β-phase (with a space group *C*2/*c*), and (iii) a high-temperature (>1450 °C) α-phase structure (with a space group *P*2).[34,38,39] Since the synthesis temperature (400−800 °C, Table S1) of crystalline Li−Ta−O coating materials is usually lower than 1450 °C, the formation of the high-temperature α-phase of Li_3TaO_4 can be excluded from the composition of typical Li−Ta−O coating materials. Therefore, we speculate that the ordered β-phase *C*2/*c* Li_3TaO_4 phase can be the other constituent of the coating material together with the *R*3*c* $LiTaO_3$ phase. The ordered *C*2/*c* Li_3TaO_4 shows zigzag chains formed by the edge-sharing TaO_6 octahedra surrounded by Li ions (lower panel of Figure 2). Li_3TaO_4 contains eight

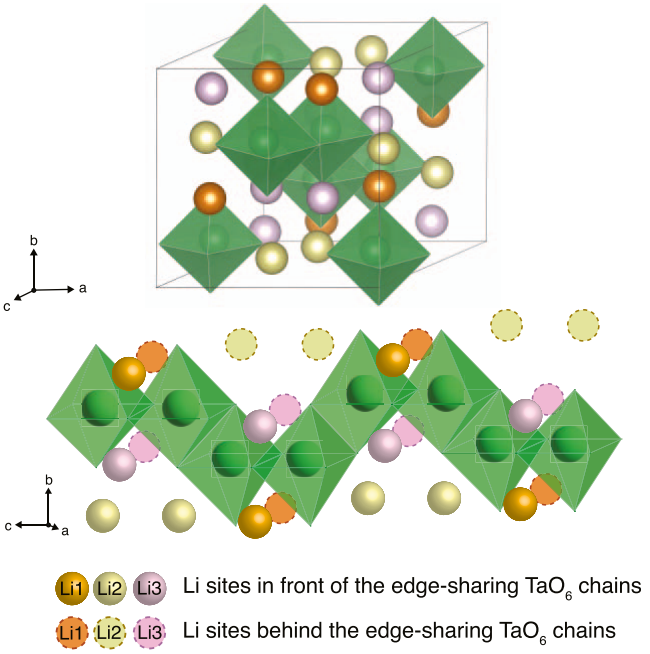

Figure 2. Structure of β-Li_3TaO_4 in the *C*2/*c* space group. Unique Li sites are labeled and shown with different colors. The lower panel shows edge-sharing (green) TaO_6 octahedra zigzag along the *c*-direction. Li environments in β-Li_3TaO_4 are highlighted in Figure S2c.

independent crystallographic sites (three Li, one Ta, and four O) in the unit cell,[40,41] which denotes the substantial difference in terms of local arrangements compared to *R*3*c* $LiNbO_3$, $LiTaO_3$, and $I\bar{4}3m$ Li_3NbO_4 displaying a unique Li site.

3. PHASE EQUILIBRIA AND ELECTROCHEMICAL STABILITIES OF LI−NB−O AND LI−TA−O COATING MATERIALS

Figure 3a,b shows the experimental binary phase diagrams of Li_2O−Nb_2O_5 and Li_2O−Ta_2O_5 systems in the composition range spanning from 40 to 62 mol % Li_2O.[24,33,42]

In Figure 3a, an exceeding (decreasing) Li_2O content into $LiNbO_3$ leads to the formation of a secondary phase, Li_3NbO_4 ($LiNb_3O_8$), that coexists with $LiNbO_3$ over a large range of composition. In Figure 3b, Li_3TaO_4 appears as a secondary phase with $LiTaO_3$ in the Li_2O-rich regions.

Figure 3c,d shows the computed (@r^{2}SCAN) phase diagrams at 0 K of Li_2O−Nb_2O_5 and Li_2O−Ta_2O_5 pseudo-binary lines including all experimentally known compositions. Green circles show the lowest-energy structures computed by DFT, while phases predicted as metastable by DFT but identified experimentally are shown by yellow circles. $Li_8Ta_2O_9$ has been excluded from Figure 3d due to the unavailability of accurate structural information. As for the disordered Li_3MO_4 (M = Nb, Ta), 32 unique orderings of Li/M have been generated for each composition using a ~2 × 2 × 1 supercell model (including 4 f.u.). Red squares show the formation energies of each Li/M ordering.

Among all competing phases, *R*3*c* $LiNbO_3$ and $I\bar{4}3m$ Li_3NbO_4 lie on the Nb_2O_5-Li_2O convex hull—the convex envelope of structures with the lowest formation energies. Therefore, any Li-rich compositions of $LiNbO_3$ (addition of Li_2O to $LiNbO_3$) will be a mixture also containing Li_3NbO_4 and in excellent agreement with Figure 3a. Similarly, *R*3*c* $LiTaO_3$ and *C*2/*c* Li_3TaO_4 are the most stable phases in the Ta_2O_5−Li_2O convex hull. Note, the formation energy of $LiTa_3O_8$ falls slightly above (~7 meV atom^{-1}) the convex hull set by Ta_2O_5 and $LiTaO_3$. This is in agreement with the absence of the $LiTa_3O_8$ phase as observed in the experiments, where only Ta_2O_5 and $LiTaO_3$ phases form under Li-

https://doi.org/10.1021/acs.chemmater.3c01197
Chem. Mater. XXXX, XXX, XXX−XXX

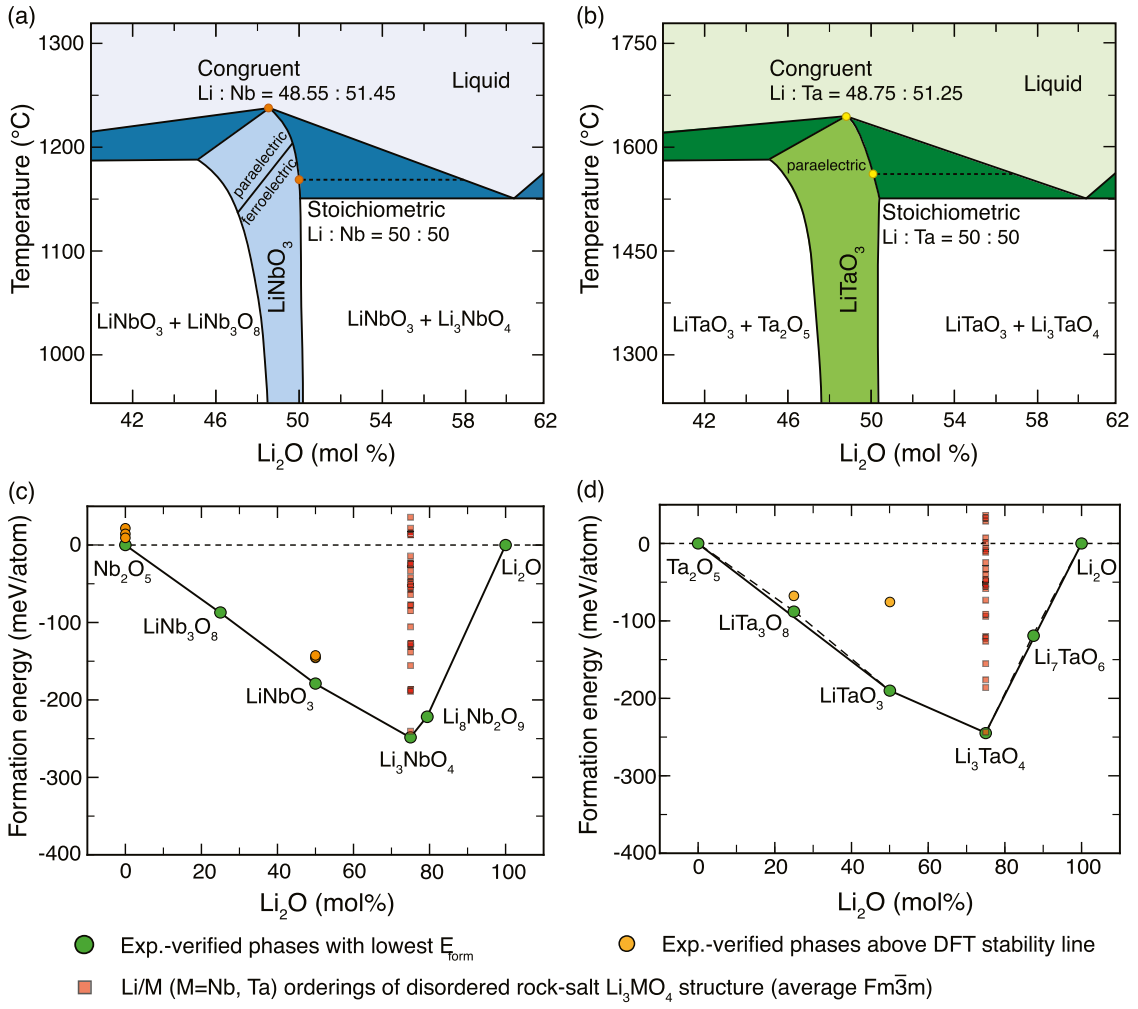

Figure 3. Phase diagrams of (a) Li_2O−Nb_2O_5 and (b) Li_2O−Ta_2O_5 pseudo-binary systems redrawn from previous experimental data.[24,33,42] The melting points of $LiNbO_3$ and $LiTaO_3$ are ∼1240 and ∼1650 °C, respectively.[33] Phase diagrams of (c) Li_2O−Nb_2O_5 and (d) Li_2O−Ta_2O_5 computed from DFT (r^{2}SCAN) at 0 K. Metastable or unstable Li/M orderings of Li_3MO_4 (M = Nb, Ta) are marked by red squares. The dashed line in panel (d) is a guide for the eye to show that $LiTa_3O_8$ sits slightly above the stability line formed by Ta_2O_5 and $LiTaO_3$.

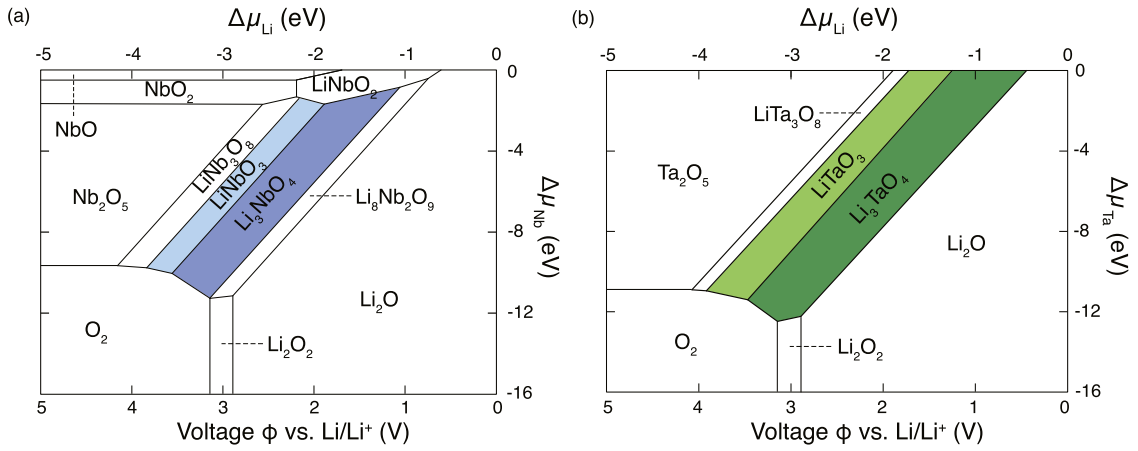

Figure 4. DFT-computed (with r^{2}SCAN and at 0 K) stability regions of niobate and tantalate phases in (a) Li−Nb−O and (b) Li−Ta−O domains. Thermodynamically stable regions are labeled, of which $LiNbO_3$, Li_3NbO_4, $LiTaO_3$, and Li_3TaO_4 are highlighted with different colors. Stable phases feature as a function of changes in the chemical potential ($\Delta\mu_{Li}$, $\Delta\mu_{Nb}$, and $\Delta\mu_{Ta}$) of Li, Nb (or Ta) referenced to their standard elemental states. Variations of $\Delta\mu_{Li}$ can be easily converted into voltages (see the main text).

poor conditions.[24,42] The computed phase diagrams of Figure 3 can qualitatively and quantitatively reproduce experimental observations.

To evaluate the electrochemical stability windows of these coating materials, we construct ternary Li−M−O (M = Nb, Ta) phase diagrams based on the elemental chemical potential changes, $\Delta\mu_{Li}$ and $\Delta\mu_M$, as

https://doi.org/10.1021/acs.chemmater.3c01197
Chem. Mater. XXXX, XXX, XXX−XXX

Table 1. Computed Electrochemical Stability Windows (in V) of Coating Materials, and Their Reaction Energies ΔE_{rxt} (meV atom^{-1}) with Different Positive Electrodes and Solid Electrolyte Chemistries Obtained from Previous Computational Works[43,44a]

	stability window		ΔE_{rxt}//cathode[43]				ΔE_{rxt}//SE[44]	
coating	red.	ox.	NMC	LCO	LMO	LFP	Li_3PS_4	LLZO
$LiNbO_3$	1.89	3.86	−4/0	0/0	0/−21	−23/−35	−155	−76
Li_3NbO_4	1.06	3.58					−132	−4
$LiTaO_3$	1.25	3.94	0/0	0/0	0/−7	−20/−24	−49	−68
Li_3TaO_4	0.44	3.55					−64	−3

[a]Red. and Ox. are for reductive (anodic) stability and oxidative (cathodic) stability, respectively. NMC is the abbreviation for $LiNi_xMn_yCo_{1-x-y}O_2$, LCO for $LiCoO_2$, LMO for $Li_2Mn_2O_4$, LFP for $LiFePO_4$, and LLZO for $Li_7La_3Zr_2O_{12}$. Values of ΔE_{rxt}//cathode are reaction energies of full/half-lithiated cathodes and coating interfaces.

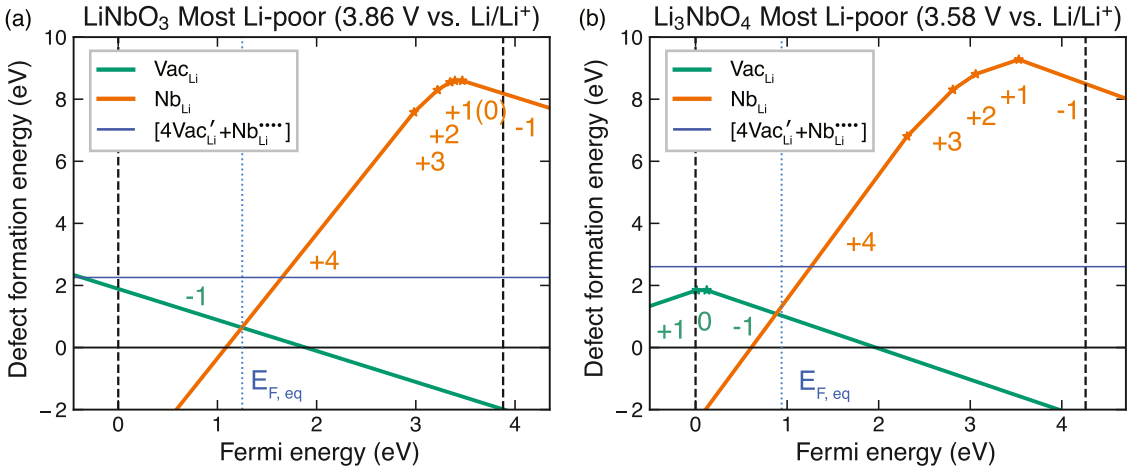

Figure 5. Computed formation energies ΔE_D of intrinsic point defects in (a) $LiNbO_3$ and (b) Li_3NbO_4 vs. Fermi energy and under the most Li-poor conditions. The chemical potentials for panel (a) were defined by the equilibrium $LiNbO_3$−$LiNb_3O_8$−O_2 ($\Delta\mu_{Li} = -3.86$ eV), and (b) by the Li_3NbO_4−$LiNbO_3$−O_2 equilibrium ($\Delta\mu_{Li} = -3.58$ eV). Fermi energy is referenced to the valence-band maximum (VBM). The band gaps of ∼3.88 eV for $LiNbO_3$ and ∼4.26 eV for Li_3NbO_4 set maximum values of the Fermi energy.

seen in Figure 4. All competing phases available in the ICSD were included.

The feasible ranges of $\Delta\mu_{Li}$ and $\Delta\mu_M$ in which $LiMO_3$ and Li_3MO_4 are thermodynamically stable are shown by colored regions in Figure 4a,b. $\Delta\mu_{Li}$ is the Li chemical potential (μ_{Li}) referenced to the chemical potential of Li metal (μ^0_{Li}). μ_{Li} is converted using the Nernst equation into voltages (versus Li/Li$^+$), $\phi = \frac{\mu^0_{Li} - \mu_{Li}}{eF} = -\frac{\Delta\mu_{Li}}{eF}$.

At more negative potential ($\Delta\mu_{Li}$) of Figure 4, which is more positive voltage vs. Li/Li$^+$, $LiNbO_3$ ($LiTaO_3$) is in direct equilibrium with $LiNb_3O_8$ ($LiTa_3O_8$) and in agreement with the phase diagram of Figure 3. This condition is said to be Li-poor or oxidative and can be realized, for example, when the coating material interfaces with a high-voltage cathode material, such as >4.20 V vs. Li/Li$^+$ in $LiNi_xMn_yCo_{1-x-y}O_2$, NMC. The Li-poor conditions can also be mimicked by a deficiency of Li precursors during synthesis. In contrast, at more positive potentials (lower voltages vs. Li/Li$^+$), $LiNbO_3$ ($LiTaO_3$) is in equilibrium with Li_3NbO_4 (Li_3TaO_4). This condition sets a chemically reducing environment (or Li-rich). From a synthesis point of view, this situation can be achieved by adding an excess of Li precursors or reacting with Li resources within cathodes.

The computed (@r^{2}SCAN) electrochemical stability windows of $LiMO_3$ and Li_3MO_4 are summarized in Table 1, which are in good agreement with previous reports.[44] $LiNbO_3$, $LiTaO_3$, Li_3NbO_4, and Li_3TaO_4 show relatively poor reducing (cathodic) stabilities toward low-voltage electrode materials, with the lowest voltage (∼0.44 V vs. Li/Li$^+$) hit by Li_3TaO_4. Similarly, $LiNbO_3$ and $LiTaO_3$ show low-oxidative (anodic) limits below 4 V vs. Li/Li$^+$ (see Table 1). Furthermore, the computed values of anodic limits of Li_3NbO_4 and Li_3TaO_4 appear slightly lower than their $LiMO_3$ analogues.

It is important to show whether the coating materials will mix spontaneously with the most common cathode electrodes, such as $LiCoO_2$ (LCO), $LiMn_2O_4$ (LMO), $LiNi_xMn_yCo_{1-x-y}O_2$ (NMC), and $LiFePO_4$ (LFP), or electrolytes, e.g., Li_3PS_4 and $Li_7La_3Zr_2O_{12}$ (LLZO). The ΔE_{rxt} of eq 1 is determined by the mixing ratio x providing the largest enthalpy of mixing[43]

$$\Delta E_{rxt} = \min_{x \text{ in } [0,1]}\{E_{pd}[xc_a + (1-x)c_b] - xE(c_a) - (1-x)E(c_b)\} \quad (1)$$

where E_{pd}, $E(c_a)$, and $E(c_b)$ are the DFT energies of the mixed phase, electrode (or electrolyte) material c_a, and coating material c_b, respectively. From Table 1, niobates and tantalates exhibit very low chemical reactivity (ΔE_{rxt}) with most oxide-based positive electrodes.[43] A low chemical reactivity with high-voltage electrodes is further enhanced if these niobates and tantalates are crystalline instead of amorphous.

When paired with thiophosphate SEs, i.e., Li_3PS_4 in Table 1, the large ΔE_{rxt} suggests that niobates may not be as stable as tantalates with thiophosphate SEs. However, the limited reactivity of tantalates compared to niobates may be explained by the lack of reported compounds containing Ta and S in contrast to more studied phases incorporating Nb and S.

4. INTRINSIC DEFECTS IN LI−NB−O AND LI−TA−O COATINGS

As shown in the phase diagram (Figure 3a), the congruent composition of $LiNbO_3$ corresponds to ∼48.55 mol % Li_2O and 51.45 mol % Nb_2O_5, with a [Li]/[Nb] ratio equal to 0.94, indicating a Li deficiency of ∼6% in $LiNbO_3$.[45] Previously, the

https://doi.org/10.1021/acs.chemmater.3c01197
Chem. Mater. XXXX, XXX, XXX−XXX

nonstoichiometry in $LiNbO_3$ was explained by three possible defect models: (i) lithium and oxygen vacancy, $[Li]_{1-2x}Nb[O]_{3-x}$, (ii) lithium vacancy and niobium antisite, $[Li]_{1-5x}[Nb_{Li}]_xNbO_3$, and (iii) niobium vacancy and niobium antisite, $Li[Nb_{Li}]_{5x}[Nb]_{1-4x}O_3$.[23,33] Model (i) can be immediately excluded as the density of the nonstoichiometric phase was found to increase with decreasing lithium content.[22,46]

To date, model (ii) is the most accepted to explain the nonstoichiometry of $LiNbO_3$. X-ray and neutron diffraction,[22,47] and solid-state nuclear magnetic resonance[48] experiments of $LiNbO_3$ suggested that ~1% of the Li sites are occupied by Nb, and ~4% of the Li sites are vacant. This ratio of 1:4 is in line with the formation of a complex charge-neutral defect encompassing one Nb antisite defect ($Nb_{Li}^{\bullet\bullet\bullet\bullet}$) accompanied by four Li vacancies (Vac_{Li}') using the Kröger–Vink notation. First-principles calculations confirmed that model (ii) is preferred compared to model (iii) under both Li-rich and Li-poor conditions.[49] Donnerberg et al.[50] investigated cation vacancies in $LiNbO_3$ and showed that the formation of Nb vacancies Vac_{Nb}'''' is less favorable than the formation of Li vacancies Vac_{Li}'.

As both $LiNbO_3$ and Li_3NbO_4 are reported in the Li–Nb–O coating layer,[15,17,28] here, we extend our defect analysis to Li_3NbO_4. Computational studies on the stability of charge-neutral defects in Li_3NbO_4 and $LiNbO_3$ suggested that a Li/Nb antisite neutral complex and Li-Frenkel defects could exist.[49,51] Therefore, we investigate the stability of Li vacancies (Vac_{Li}) and Nb antisites (Nb_{Li}), as well as the charge-neutral complex defects [$4Vac_{Li}' + Nb_{Li}^{\bullet\bullet\bullet\bullet}$] of model (ii).

Figure 5 plots the computed (@r^{2}SCAN) formation energies ΔE_D of isolated Li vacancies (Vac_{Li}) and Nb antisites (Nb_{Li}) in $LiNbO_3$ and Li_3NbO_4 following eq 2. Results of isolated point defects in $LiTaO_3$ and Li_3TaO_4 are provided in Figure S7 and Tables S8, S9. ΔE_D values are plotted as a function of the Fermi energy (E_{Fermi}). We referenced the absolute values of the Fermi energy to the energy of the valence-band maximum (VBM) of each bulk structure. The slopes of the defect lines represent different charge states of the defect (q in eq 2).

High-temperature calcination facilitates the consumption of Li resources in positive electrode materials, hence setting a condition of Li-rich for $LiNbO_3$ and Li-poor for Li_3NbO_4 at the coexistence of these two phases (Section 6). Upon charging, the availability of free Li in the cathode sets Li-rich conditions for the coating components (see Figure S6). Therefore, it is crucial to investigate the formation of defects under different chemical/electrochemical conditions of the coating.

Solid lines in Figure 5 represent the ΔE_D values under the most Li-poor (oxidative) conditions for $LiNbO_3$ ($LiNbO_3$–$LiNb_3O_8$–O_2 equilibrium) and Li_3NbO_4 (Li_3NbO_4–$LiNbO_3$–O_2 equilibrium). The defect formation energies under the most Li-rich (reducing) conditions of $LiNbO_3$ and Li_3NbO_4 can be found in Figure S6. By definition, values of ΔE_D must be always positive quantities. In Figure 5a,b at specific Fermi energies (<1 and >2.5 eV), the computed ΔE_D values are negative. This indicates that these defects are unstable in the phase space set by the chemical potentials of Li and Nb (Figure 4).

Based on the temperature of calcination of coating materials (~1000 K),[15,16,28] both $LiNbO_3$ and Li_3NbO_4 phases coexist in the crystalline niobate coatings. Room-temperature (300 K) data are shown in Tables S6 and S7. Vertical dotted (blue) lines are the equilibrium Fermi energy ($E_{F,eq}$) under the Li-poor condition. Note, the equilibrium Fermi energy informs about the availability of electrons (or holes) in the coating material.[52,53]

Under the most Li-poor condition for $LiNbO_3$ (Figure 5a), the equilibrium Fermi Energy ($E_{F,eq}$) is ~1.271 eV at 1000 K. The defect formation energies for Vac_{Li}' and $Nb_{Li}^{\bullet\bullet\bullet\bullet}$ are 0.62 and 0.74 eV, resulting in defect concentrations at 10^{19} and 10^{18} cm^{-3}, respectively. The carrier (hole) concentration reaches the order of 10^{15} cm^{-3}. Under the most Li-rich condition in $LiNbO_3$ (Figure S6a), $E_{F,eq}$ is shifted to 2.89 eV at 1000 K, where ΔE_D for Vac_{Li}' and $Nb_{Li}^{\bullet\bullet\bullet\bullet}$ are 0.96 and 1.09 eV, respectively. The corresponding defect concentrations decrease to 10^{17} and 10^{16} cm^{-3}. This trend shows that both Li vacancies and Nb antisites are less favored in the Li-rich condition of $LiNbO_3$ at the same temperature, resulting in a decrease in defect concentrations. $LiNbO_3$ in Li-rich conditions displays a higher free-electron concentration around 10^{16} cm^{-3}.

Under the most Li-poor condition in Li_3NbO_4 at 1000 K (Figure 5b), $E_{F,eq}$ is at 0.93 eV. The corresponding ΔE_D for Vac_{Li}' and $Nb_{Li}^{\bullet\bullet\bullet\bullet}$ are 1.04 and 1.28 eV, much higher than those of $LiNbO_3$. The defect concentrations of Vac_{Li}' and $Nb_{Li}^{\bullet\bullet\bullet\bullet}$ are at 10^{17} and 10^{16} cm^{-3}, respectively. The charge (hole) carrier concentration is 10^{17} cm^{-3}. Under the most Li-rich condition for Li_3NbO_4 at 1000 K (Figure S6b solid lines), $E_{F,eq}$ moves to 2.85 eV, where ΔE_D for Vac_{Li}' is 1.61 eV, and for less probable defects $Nb_{Li}^{\bullet\bullet}$ and $Nb_{Li}^{\bullet\bullet\bullet}$, 1.71 and 1.75 eV, respectively. This indicates that Nb_{Li} with lower charge states are likely to be more stable than $Nb_{Li}^{\bullet\bullet\bullet\bullet}$ in Li_3NbO_4 under such conditions. But the defect concentrations of Li vacancies and Nb antisites are only at 10^{14} and 10^{13} cm^{-3} and hence several orders of magnitude lower than those in the Li-poor condition. The free-electron concentration of Li_3NbO_4 in the Li-rich condition is only around 10^{13} cm^{-3}.

We now analyze the stability of neutral defect complex in $LiMO_3$ and Li_3MO_4 (M = Nb, Ta) comprising of four Li vacancies together with one Nb (Ta) antisite, thereafter indicated as [$4Vac_{Li}' + M_{Li}^{\bullet\bullet\bullet\bullet}$]. The spatial arrangement of antisite and Li vacancies in $LiNbO_3$ and Li_3NbO_4 may vary and affect the relative stability of these defects. To this end, we investigated a number of possibilities (spatial orderings), whose details are in Section S3. Defect complex models in Li_3TaO_4 with three unique crystallographic Li sites were constructed for each Li site. The configuration where the Li2 site is exchanged by a Ta atom shows the lowest formation energy. Table 2 summarizes the ΔE_D of lowest-energy configurations among all defect models under Li-poor conditions.

As shown in Table 2, values of ΔE_D's of neutral defect complexes in $LiMO_3$ and Li_3MO_4 are comparatively lower than the sum of the individual point defects (last column). For example, the sum of defect formation energies for $4Vac_{Li}'$ and $Nb_{Li}^{\bullet\bullet\bullet\bullet}$ in $LiNbO_3$ at $E_{F,eq}$ under the Li-poor condition is ~3.23

Table 2. Computed r^{2}SCAN Defect Formation Energies (ΔE_D in eV) of Neutral Antisite Defect Complexes ([$4Vac_{Li}' + M_{Li}^{\bullet\bullet\bullet\bullet}$]) Compared to the Sum of Isolated Defects ($4Vac_{Li}' + M_{Li}^{\bullet\bullet\bullet\bullet}$, M = Nb, Ta)[a]

coating	[$4Vac_{Li}' + M_{Li}^{\bullet\bullet\bullet\bullet}$]	$4Vac_{Li}' + M_{Li}^{\bullet\bullet\bullet\bullet}$
$LiNbO_3$@Li-poor	2.26	3.23
Li_3NbO_4@Li-poor	2.61	5.43
$LiTaO_3$@Li-poor	2.09	3.28
Li_3TaO_4@Li-poor	2.31	6.05

[a]Calculations of antisite defect complexes [$4Vac_{Li}' + M_{Li}^{\bullet\bullet\bullet\bullet}$] used large supercell models of $LiMO_3$ ($Li_{64}M_{64}O_{192}$) and Li_3MO_4 ($Li_{96}M_{32}O_{128}$). The Li-poor reference states are provided in Table S10.

https://doi.org/10.1021/acs.chemmater.3c01197
Chem. Mater. XXXX, XXX, XXX–XXX

eV, while that of the complex neutral defect is ~2.26 eV. This indicates the favorable enthalpy gain of forming a stable complex as discussed by Li et al.[54] In the reducing (Li-poor) conditions, the minimum ΔE_D of the defect complex in Li_3NbO_4 is ~2.61 eV.

5. LI-ION MOBILITY IN $LIMO_3$ AND LI_3MO_4 COATINGS

In this section, we address the mobility of Li ions in $LiMO_3$ and Li_3MO_4 by performing inexpensive but empirical SoftBV predictions, followed by accurate first-principles nudged elastic band (NEB) simulations.

Figure 6 shows the bond valence site energy (BVSE) landscape computed with SoftBV for each bulk structure

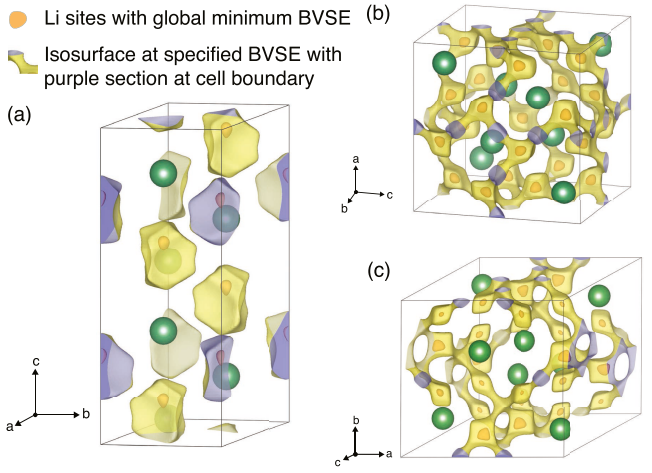

Figure 6. BVSE landscapes obtained from SoftBV of (a) *R*3*c* $LiMO_3$ (M = Nb, Ta), (b) *I*4̄3*m* Li_3NbO_4, and (c) *C*2/*c* Li_3TaO_4. Values of volumetric isosurfaces are set at 2000, 700, and 700 meV above the global minimum-energy set by Li sites, within $LiNbO_3$ ($LiTaO_3$), Li_3NbO_4, and Li_3TaO_4, respectively. Li sites setting global minima are colored in orange. Nb and Ta atoms are shown in green and serve as a guide for the eye.

whose volumetric isosurfaces are set to 2000 meV (in $LiMO_3$) and 700 meV (in Li_3MO_4), above the global minimum of Li-site energy computed by SoftBV. From the disconnected isosurfaces seen in Figure 6a, it is unlikely for Li ions to migrate in the defect-free crystalline phases of $LiNbO_3$ or $LiTaO_3$, as no Li "channels" are formed between adjacent sites. Figures 6b and S8 clearly depict extended percolating Li-diffusion channels of Li_3NbO_4. For the ordered β-phase Li_3TaO_4, Figures 6c and S9 show the percolating networks of Li ions. Insightful illustrations of the migration environments near the crystallographic Li1, Li2, and Li3 sites are provided in Figure S13a–c.

From the SoftBV analysis, the percolating migration barriers—that give rise to a net transport of Li ions within the coating material—were further investigated using NEBs coupled with DFT@r^{2}SCAN. Three main types of Li^+ migration pathway can be envisioned as below.

1. Pathway Vac_{Li}: One Li vacancy Vac'_{Li} (low-vacancy limit) was introduced and compensated by a background charge (in the form of jellium).
2. Pathway $4Vac_{Li} + M_{Li}$ (M = Nb, Ta): One Li vacancy Vac'_{Li} of the four vacancies of the charge-neutral defect complex $[4Vac'_{Li} + M^{\bullet\bullet\bullet\bullet}_{Li}]$ migrates.
3. Pathway $4Vac^{\triangle}_{Li} + M_{Li}$: One Li vacancy Vac'_{Li} of the four vacancies of the charge-neutral complex defect $[4Vac'_{Li} + M^{\bullet\bullet\bullet\bullet}_{Li}]$ migrates. All of the other three Vac'_{Li} were located near the migration event.

Based on these three distinct pathways, distinct migration models were identified by looking at the coordination environment of the migrating Li-ion (Figures 1 and 2). Values of computed migration barriers are summarized in Figure 7 and Table S11.

From Figure 7a,c, no matter which of the three pathways are chosen, the predicted migration barriers in $LiNbO_3$ and $LiTaO_3$ are consistently larger than 1100 meV. This data clearly demonstrates that Li-ion transport in $LiNbO_3$ and $LiTaO_3$ relying on intrinsic defects cannot guarantee sufficient Li-ion transport.

In particular, for $LiNbO_3$ and $LiTaO_3$, the Li-ion migration barriers in the low-vacancy limit model (Vac_{Li}) are 1273 and 1240 meV, respectively, in agreement with previous experimental results.[13,19] To investigate whether the presence of the neutral defect complex ($[4Vac'_{Li} + M^{\bullet\bullet\bullet\bullet}_{Li}]$) can lower the high migration barriers of crystalline $LiNbO_3$ ($LiTaO_3$), we studied the Li-ion migration in the vicinity of these defects (see Figure S11b,c). As shown in Figure 7a,c, migration barriers are still as high as ~1296 meV for $LiNbO_3$ and ~1406 meV for $LiTaO_3$. The computed migration energies of Li-ion in congruent $LiNbO_3$ (~1296 meV) appear in excellent agreement with the experimental values (~1300 meV).[26,27]

Starting from the hypothesis that the presence of Li vacancies near the migrating Li-ion may lower its migration barriers, in Li migration models labeled as $4Vac^{\triangle}_{Li} + Ta_{Li}$, we forced all four Li vacancies to be close to the Li migration pathway (Figure S11d). Although the activation barriers (~1126 meV for $LiNbO_3$ and ~1146 meV for $LiTaO_3$) are slightly lower than in the other cases, such barriers are still too high to achieve reasonable Li-ion transport across the coating layer.

Li_3NbO_4 and Li_3TaO_4 exhibit much more promising transport properties with lower activation barriers, on average lower than 700 meV (Figure 7b,d). For example, in Li_3NbO_4, one Li vacancy can migrate to its two first NNs (~467 meV), four second NNs (~543 meV), and one third NN (~701 meV, shown in Figure S12b) sites, respectively. Among 11 distinct pathways considered between three types of Li sites in Li_3TaO_4, eight migration barriers are consistently lower than 700 meV (see Table S11). Therefore, in Li_3NbO_4 and Li_3TaO_4, several migration pathways may enable macroscopic diffusion of Li ions (Figures S8 and S9).

In analogy to $LiMO_3$, we also explore the Li migration in Li_3MO_4 (M = Nb, Ta) in the vicinity of the M_{Li} antisite and four Li vacancies. The computed paths of these Li migrations are shown in Figures S12d and S13d–f, respectively. From Figure 7b, in Li_3NbO_4, the Li-ion migration barriers generally increase in the proximity of Nb antisite defects when compared to the migration of a diluted Li vacancy (models Vac_{Li} in Figure 7b). However, most pathways in Figure 7b still show relatively low barriers (models 1a, 1b, and 1c with barriers of 535, 502, and 522 meV). A similar trend is found for Li_3TaO_4 as depicted in Figure 7c. In both Li_3NbO_4 and Li_3TaO_4, specific arrangement of Li vacancies can lead to a sudden increase in the migration barriers, even beyond 1200 meV (see Figure 7b,c).

This variation in the Li migration barriers is introduced by the immediate crystallographic environment of niobates (tantalates) and the proximity of the Li migration event to the complex antisite defect. In $LiMO_3$ (M = Nb, Ta), the NEB barriers for Li ions migrating in the presence of a defect complex vary slightly.

https://doi.org/10.1021/acs.chemmater.3c01197
Chem. Mater. XXXX, XXX, XXX−XXX

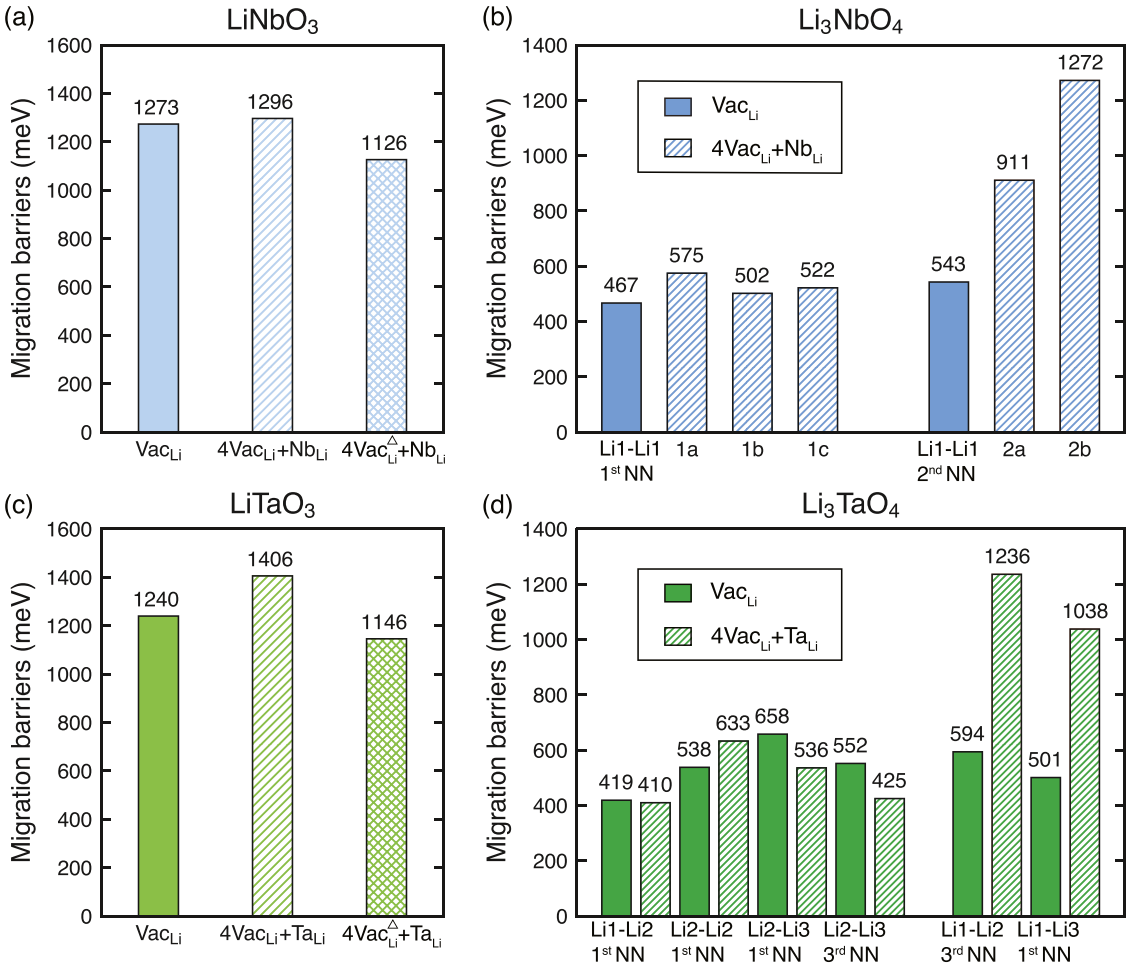

Figure 7. Li-ion migration barriers computed with NEB@r^{2}SCAN in (a) $LiNbO_3$, (b) Li_3NbO_4, (c) $LiTaO_3$, and (d) Li_3TaO_4 supercell structures. In these structures, the environment of Li ions is set in terms of nearest neighbors, NNs (Figures 1 and 2). Filled bars show migration barriers computed in the low-vacancy limit (incorporating one Vac'_{Li} per supercell). Hatched bars show migration barriers of models incorporating neutral complex antisite-vacancy defects ($4Vac_{Li} + M_{Li}$). Bars with crossed patterns show migration barriers for $LiMO_3$ in the presence of the antisite defect complex, with all Li vacancies near the migration pathways and indicated as $4Vac^{\triangle}_{Li} + M_{Li}$. Configurations of all pathways are provided in Figures S11−S13.

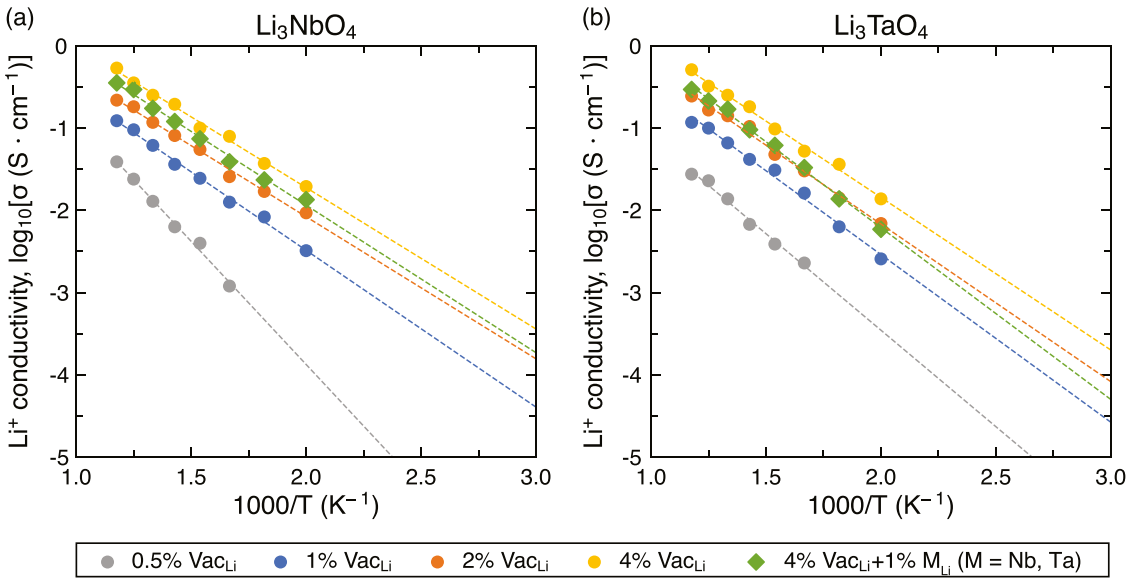

Figure 8. Arrhenius plots of Li-ion conductivities in (a) Li_3NbO_4 and (b) Li_3TaO_4 obtained from MTP-MDs trained on different defect types and concentrations. The temperatures modeled range from 500 to 850 K, except for model 0.5%. Dashed lines are the Arrhenius fits whose migration energies are in Table S13.

https://doi.org/10.1021/acs.chemmater.3c01197
Chem. Mater. XXXX, XXX, XXX−XXX

This is because the closely packed structures of $LiMO_3$ are very symmetric and structural changes introduced by point defects cause minimal variations in the migration environment and hence the Li-ion migrating barriers. In Li_3MO_4, the migration barriers of a Li vacancy (low-vacancy limit model) appear very sensitive to the migration environment as reflected in Figure 7b,d. In the structures of Li_3NbO_4 (tetramer of Nb octahedra) and Li_3TaO_4 (zigzag chain of Ta octahedra) of Figures 1b and 2, the high-valence Nb^{5+} and Ta^{5+} ions arrange sparsely, in a way to provide additional voids enabling facile Li^+ migration. In addition to the local environment, the introduction of the antisite defect complex will affect the Li migration pathways by either reducing the Li^+-Li^+ repulsion near the 4 Li vacancies or increasing the repulsion for pairs $Li^+-M_{Li}^{5+}$.

So far, the computed migration barriers of Figure 7, Li_3MO_4 (M = Nb, Ta), suggest facile Li-ion transport compared to $LiMO_3$. To gain more insight into the complex behavior of Li-ion transport in Li_3MO_4 (M = Nb, Ta), we perform machine-learning molecular dynamics (MDs) simulations based on the moment tensor potential (MTP) method.[55] In the MTP, we explore the effect of different concentrations of Vac'_{Li}, set to 0.5, 1, 2, and 4%. As calculated in Section 4, the ΔE_D values of neutral defect complexes in Li_3MO_4 are comparable with $LiMO_3$. Here, we only considered the case of 4% Li vacancies and 1% M antisites in Li_3MO_4, with the MTP-MD simulations performed in the most favorable defect models of Li_3NbO_4 and Li_3TaO_4 (see Figures S12c and S13e).

Figure 8 shows the Li-ion transport properties from MTP-MD simulations. Predicted migration barriers can be derived from the Arrhenius fits of Figure 8, shown in Table S13. In Figure 8, by including 0.5% Li vacancies in Li_3NbO_4, we achieved migration barriers ~622 meV, in agreement with experimental values (~580−850 meV) of crystalline Li_3NbO_4 and NEB barriers of Figure 7.[19,29,56] Unsurprisingly, as the concentration of Li vacancies in Li_3NbO_4 increases, the inferred migration barriers of Li_3NbO_4 of 2 and 4% Li vacancies decrease significantly to ~400 meV. Likewise, the Li-ion conductivities increase greatly by three to five orders of magnitude by increasing the Vac_{Li} from 0.5 to 4.0%. As shown in Figure 8b, the ionic conductivities of Li_3TaO_4 are similar to those of Li_3NbO_4. The extrapolated Li migration barrier in Li_3TaO_4 with 0.5% Li vacancies is estimated to ~527 meV, in agreement with the experimental measurements (~550 meV in $Li_{2.98}Ta_{1.004}O_4$).[57] Similar to Li_3NbO_4, as the concentration of Li vacancies increases, Li_3TaO_4 exhibits improved conduction properties.

In the presence of Nb or Ta antisite defect complexes, the Li-ion conduction of Li_3MO_4 of 4% Li vacancies and 1% M antisites is comparable with the ionic conductivity predicted in a model system with 4% Li vacancies. These results show that the M_{Li} antisite defects may not significantly affect Li-ion transport in Li_3MO_4, but M_{Li} defects ensure the availability of Li vacancies. The migration barriers of Figure 7 support these observations.

6. DISCUSSION

To improve the cathode−electrolyte interfacial stability, extend the oxidation potential of electrolytes, and increase the longevity of lithium-ion batteries, coating materials are usually applied to positive electrode materials.[2] Commonly used coating materials are niobates and tantalates.[9]

Niobate coating materials are typically synthesized using wet-chemical protocols. In these syntheses (see Table S1), the temperature of calcination mainly affects the crystallinity of $LiNbO_3$ and the distribution of $LiNbO_3$ with secondary phases, as revealed by X-ray diffraction and transmission electron microscopy experiments.[15−17]

As the temperature increases, up to four "stages" of calcination may be involved in the fabrication of these Li−Nb−O materials (Table S1),[10,16,28,36] which are as follows.

1. At low calcination temperatures (<400 °C), there only exists an amorphous $LiNbO_3$ phase, which display high Li-ion conductivities ($10^{-5}-10^{-6}$ S cm^{-1}).
2. At intermediate temperatures (400−650 °C), the crystalline $LiNbO_3$ phase coexists with the disordered rock-salt Li_3NbO_4 phase.
3. At high temperatures (650−750 °C), a mixture of the crystalline $LiNbO_3$ phase with the ordered $I\bar{4}3m$ Li_3NbO_4 phase is identified.
4. At temperature exceeding 750 °C, the niobate coating is composed of a single ordered $I\bar{4}3m$ Li_3NbO_4 phase. Therefore, at this stage, all of the $LiNbO_3$ phase is transformed into Li_3NbO_4.

The conversion temperatures between the Li−Nb−O phases mentioned above can have slight variations when the amount of precursors used in the synthesis and the calcination time vary. As an example, in the recent work of Xin et al.,[28] the niobate coating material contains only Li_3NbO_4 when calcinated for 3 h at ~690 °C. In contrast, Zhang et al.[15] characterized that a Li−Nb−O coating still displays crystalline $LiNbO_3$ and Li_3NbO_4 phases after calcination at ~700 °C for 10 h. This analysis suggests that niobate coating materials, commonly accepted as "$LiNbO_3$", may coexist with Li-rich materials, such as Li_3NbO_4 (see Figures 3a and 4a). From our simulations, we extend these findings to tantalate coatings that may contain varying mixtures of $LiTaO_3$ and Li_3TaO_4.

From this investigation emerged that selected calcination temperatures control the coexistence of $LiMO_3$ and Li_3MO_4 (M = Nb, and Ta) phases in the coating materials. The concurrence of $LiMO_3$ and Li_3MO_4 phases can promote the formation of defects within Li_3MO_4 with promising ionic conductivities. Concomitantly, the presence of $LiMO_3$ extends the oxidative resistance to higher voltages, improving the electrochemical performance of batteries. Nevertheless, if calcination temperatures exceed 750 °C, $LiMO_3$ will be fully depleted, and the exceeding Li_3MO_4 will lower the onset voltage for oxidation to ~3.6 V vs Li/Li^+.

The coexistence of $LiMO_3$ and Li_3MO_4 suggests that the functional properties of these coating materials, such as, (i) the Li-ion transport in these phases, (ii) the chemical and electrochemical stabilities (under an external bias), and (iii) the mechanical properties (not investigated here) are broadly linked to the multiphased nature of these materials. We built robust thermodynamic and kinetic models using state-of-the-art first-principles calculations to link the multiphased nature of niobates (tantalates) with their functional properties.

6.1. Intrinsic Defects in Coating Materials. Using DFT (at the r^{2}SCAN level of theory), we verified the natural occurrence of intrinsic defects in these materials. The equilibrium of $LiNbO_3$ and Li_3NbO_4 in niobates will set a Li-poor (more oxidative) condition, highly favoring the formation of a neutral antisite defect complex in Li_3NbO_4, implying the simultaneous formation of four Li vacancies and a charged $Nb_{Li}^{\bullet\bullet\bullet\bullet}$ antisite defect, i.e., $[4Vac'_{Li} + Nb_{Li}^{\bullet\bullet\bullet\bullet}]$ (Tables 2 and S10). We arrived at similar findings in Li_3TaO_4, suggesting that the coexistence of $LiTaO_3$ and Li_3TaO_4 (Li-poor condition) will

https://doi.org/10.1021/acs.chemmater.3c01197
Chem. Mater. XXXX, XXX, XXX−XXX

favor the formation of a neutral defect complex in Li_3TaO_4, i.e., $[4Vac'_{Li} + Ta^{\bullet\bullet\bullet\bullet}_{Li}]$.

In general, in $LiNbO_3$, our DFT defect formation energies suggest that the neutral defect complex, i.e., $[4Vac'_{Li} + Nb^{\bullet\bullet\bullet\bullet}_{Li}]$, is highly favored in the Li-poor condition. Isolated Li vacancies and $Nb^{\bullet\bullet\bullet\bullet}_{Li}$ antisites are also likely to form in $LiNbO_3$, with concentrations $\sim 1.39 \times 10^{19}$ and $\sim 3.46 \times 10^{18}$ cm^{-3}, respectively, at 1000 K. Characterization with neutron and X-ray diffraction,[22,47] and later solid-state nuclear magnetic resonance[48] on $LiNbO_3$ suggested that ~1% of the Li sites are occupied by Nb, and ~4% of the Li sites are vacant, hence supporting the existence of a neutral antisite defect complex and in excellent agreement with our computational models. While at the cathode interface, exchange of Nb (Ta) from the coating layer with transition metals of the positive electrode is possible;[58] here, we did not investigate the occurrence of these antisite defects.

6.2. Li-Ion Transport in Niobate and Tantalate Coatings. Subsequently, we inspected the properties of Li-ion transport (with SoftBV, NEB, and MTP-MD simulations) in the presence of defect types favored by the thermodynamic conditions in $LiNbO_3$ and Li_3NbO_4, and $LiTaO_3$ and Li_3TaO_4. In this work, we did not focus on simulating the behavior of amorphous niobates and tantalates. However, experimental investigations by Rahn et al.[26] suggested that amorphous $LiNbO_3$ synthesized in Li-poor (more oxidative) conditions exhibits better Li-ion transport (E_a = 700 meV) than amorphous $LiNbO_3$ (E_a = 830 meV) synthesized in Li-rich conditions. This observation matches our computational results, with $LiNbO_3$ and Li_3NbO_4 likely to be highly defective in Li-poor conditions.

Clearly, coating materials are effective at migrating the Li-ion if the migration barriers are within some prescribed tolerance values. Previously, the maximum tolerable migration barriers (E_a^{max}) for Li ions in coating materials were estimated using the model proposed by Chen et al.,[59] suggesting that coating layers of different thicknesses are only viable when the Li migration barriers are smaller than a maximum value E_a^{max}. Based on manufacturing data of crystalline Li−Nb−O and Li−Ta−O coatings (Table S1), we identified "reasonable" operating conditions to derive a value of E_a^{max}, which set a 10 nm coating thickness, operating at 25 °C, and at a discharge rate of 1C (1 h). This yields to E_a^{max} of ~700 meV.

In crystalline $LiNbO_3$ and $LiTaO_3$, our data suggest that the migration of Li vacancies (in the dilute regimes) remains high (>1100 meV) with or without the presence of $[4Vac'_{Li} + M^{\bullet\bullet\bullet\bullet}_{Li}]$ in the materials. These values feature consistently above the maximum tolerable barriers, ~700 meV for these coating materials. However, experimentally amorphous $LiNbO_3$ and $LiTaO_3$ both appear decent Li-ion conductors at room temperature ($\sim 10^{-5}$−10^{-6} S cm^{-1}). Therefore, future computational studies are required to elucidate the Li-ion transport properties of these amorphous phases.

The computed migration barriers in the crystalline Li_3NbO_4 (or Li_3TaO_4) phase are significantly lower (mostly <700 meV) than crystalline $LiNbO_3$ (or $LiTaO_3$). Li-ion conductivities obtained with machine-learned MDs also corroborate this finding. We claim that Li_3NbO_4 or Li_3TaO_4 are the active components in niobate or tantalate coating materials. Therefore, synthesis protocols and defect engineering remain crucial to the overall properties of these coating materials.

6.3. Low-Oxidative Stability Limits of $LiMO_3$ and Li_3MO_4. The high operating voltages ≥4.2 V vs. Li/Li^+ delivered by high nickel content layered materials, such as $LiNi_{0.8}Co_{0.1}Mn_{0.1}O_2$ (NMC811), require coating materials with matched oxidative stability windows. In Table 1, we estimated the oxidative (anodic) stabilities of all phases in niobate and tantalate coating materials. As widely applied coating materials, $LiNbO_3$ and $LiTaO_3$ show low-oxidative (anodic) limits below 4 V vs. Li/Li^+ (see Table 1), which are lower than the reported values of some phosphate coatings, such as Li_3PO_4 (~4.2 V vs. Li/Li^+) and $LiPO_3$ (~5.0 V).[44] The predicted anodic limits of Li_3NbO_4 and Li_3TaO_4 appear slightly lower than their $LiMO_3$ analogues. Indeed, the higher Li-ion transport in crystalline Li_3NbO_4 (and Li_3TaO_4) phases compared to $LiNbO_3$ (and $LiTaO_3$) can explain the limiting oxidative stabilities of Li_3MO_4 materials. Therefore, the selection of adequate calcination treatments for niobate and tantalate coatings should always ensure the concurrence of the highly conductive Li_3MO_4 component and $LiMO_3$ phases with better anodic stabilities.

Furthermore, from our calculations of intrinsic defects in the niobate and tantalate phases, the equilibrium Fermi energies, $E_{F,eq}$ (see Figure 5), can be linked to the electronic conductivity of these bulk materials.[53,60] Across all of the chemical and electrochemical environments (reducing or oxidizing) explored here, the equilibrium Fermi energies of lithium niobates and tantalates are always at least ~1 eV away from the valence or conduction bands. This indicates that intrinsic defects in lithium niobate and tantalate bulks alone may not impart significant electronic conductivities.

7. CONCLUSIONS

We investigated the structure−property relationship of lithium niobates and tantalates, which are an important class of coating materials for lithium-ion batteries. We underscored the importance of the multiphasic nature of niobate coating materials, $LiNbO_3$ and Li_3NbO_4. Similarly, tantalates appear in mixtures of $LiTaO_3$ and Li_3TaO_4.

We demonstrate that $LiNbO_3$ and Li_3NbO_4 may contain high concentrations of lithium vacancies Vac'_{Li} and antisites $Nb^{\bullet\bullet\bullet\bullet}_{Li}$ arranged into charge-neutral defect complexes, $[4Vac'_{Li} + M^{\bullet\bullet\bullet\bullet}_{Li}]$. Our simulations reveal poor Li-ion transport of crystalline $LiNbO_3$ and $LiTaO_3$ even in the presence of intrinsic defects Vac'_{Li} and a neutral antisite defect complex $[4Vac'_{Li} + M^{\bullet\bullet\bullet\bullet}_{Li}]$. In contrast, our analysis demonstrates that the secondary phases Li_3NbO_4 and Li_3TaO_4 are much better ion conductors than $LiNbO_3$ and $LiTaO_3$.

Finally, the low-oxidative (anodic) voltages of Li_3NbO_4 and Li_3TaO_4 compared to $LiNbO_3$ and $LiTaO_3$ encourage the selection of adequate calcination treatments to ensure the concurrence of both phases.

Our findings stimulate more in-depth investigations on the structure−property relationships of these highly sought coating materials.

8. METHODS

8.1. First-Principles Calculations. Density functional theory (DFT) calculations were performed using the Vienna *ab initio* Simulation Package.[61] The projector augmented wave potentials described the core electrons, and are as follows: Li 17Jan2003 $2s^1$, Nb_pv 08Apr2002 $4p^6\ 5s^1\ 4d^4$, Ta_pv 07Sep2000 $5p^6\ 6s^2\ 5d^3$, and O 08Apr2002 $2s^2\ 2p^4$.[62] The kinetic energy cutoff describing the valence electrons was set to 520 eV. The meta-GGA functional r^2SCAN approximates the exchange−correlation energy.[63] The PBE functional was used for training the machine-learned potentials,[64] as it is ~10% faster than r^2SCAN in the *ab initio* molecular dynamics (AIMDs). 5 × 5 × 5 Γ-centered *k*-point meshes were used to integrate the first Brillouin

https://doi.org/10.1021/acs.chemmater.3c01197
Chem. Mater. XXXX, XXX, XXX−XXX

zone of $LiNbO_3$ and $LiTaO_3$ (with a $R3c$ space group) and converged within 10^{-5} eV. k-point meshes of $3 \times 3 \times 3$ and $4 \times 4 \times 2$ were applied to Li_3NbO_4 ($I\bar{4}3m$) and Li_3TaO_4 ($C2/c$). In larger supercells and metals (Li, Nb, and Ta), the k-point meshes were optimized. With the exception of defect calculations, volumes, shapes, and coordinates of each structure were optimized until the interatomic forces were $\leqslant 10^{-2}$ eV Å^{-1}.

All crystal structures were taken from the Inorganic Chemical Structure Database. Disordered rock-salt structures of Li_3NbO_4 and Li_3TaO_4 were ordered by computing all possible Li/Nb (Li/Ta) arrangements at given supercell sizes.[65] O_2 gas was used as a reference for the oxygen μ_O, and was simulated by placing an oxygen dimer in a $10 \times 10 \times 10$ Å^3 box. We included O_2 vibrational contributions (~100 meV at 0 K).

As shown in Tables S2 and S3, the DFT-calculated structures of $LiNbO_3$ ($R3c$), $LiTaO_3$ ($R3c$), Li_3NbO_4 ($I\bar{4}3m$), and β-Li_3TaO_4 ($C2/c$), using the meta-GGA r^{2}SCAN exchange and correlation functional, are in much better agreement with existing experimental data on the lattice parameters and electronic band structures.[40,66−68]

8.2. Defect Formation Energies. The following intrinsic point defects were studied: Li vacancy (Vac_{Li}) and M-Li antisite (M_{Li}, M = Nb, Ta). We also investigated charge-neutral defect complexes [$4Vac'_{Li} + M^{\bullet\bullet\bullet\bullet}_{Li}$], M = Nb, Ta. Defects in $LiNbO_3$, $LiTaO_3$, Li_3NbO_4, and Li_3TaO_4 were modeled by large supercells containing 320, 320, 256, and 256 atoms, respectively. The defect formation energies $\Delta E_D(X^q)$ are calculated from eq 2

$$\Delta E_D(X^q) = E^{tot}_{defect} - E^{tot}_{bulk} - \sum_i n_i\mu_i + qE_{Fermi} + E_{corr} \quad (2)$$

where E^{tot}_{defect} and E^{tot}_{bulk} are the r^{2}SCAN energies of supercells with and without defect. μ_i is the chemical potential of species i, while n_i is the number of atoms of i added to ($n_i > 0$) or removed from ($n_i < 0$) the supercell model. μ_{Li} and μ_M were derived from the phase diagram of Li−Nb−O and Li−Ta−O (Figure S5). We explored defects with charges q: [−1, 0, and 1] for Vac_{Li} and [−1, 0, 1, 2, 3, and 4] for M_{Li}. The E_{Fermi} spans the r^{2}SCAN band gaps of the respective bulk structures. E_{corr} corrects for the electrostatic energy of charged defects interacting with their periodic images and the potential alignment for the fictitious jellium background.[69,70] The correction of ref 70 was used for lower-symmetry $LiNbO_3$, Li_3TaO_3, and Li_3TaO_4,[70] whereas we implemented ref 69 for Li_3NbO_4. The band structures computed with different GGA (PBE and PBEsol) and meta-GGA (SCAN and r^{2}SCAN) exchange and correlation functionals are shown in Figure S4. Details about the computation of defect concentrations and the identification of equilibrium Fermi energies are in refs 53, 60.

8.3. Li-Ion Migration in $LiMO_3$ and Li_3MO_4 (M = Nb, Ta). The empirical softBV analysis was used to identify the topology of Li-ion diffusion in $LiMO_3$ and Li_3MO_4.[71]

In the nudged elastic band (NEB) calculations, we used models as detailed in Section 8.2, which ensure a minimum distance ≥8 Å between image replicas.[59,72] In NEBs, spring forces were set to 5 eV Å^{-1}, and charge neutrality was imposed through a compensating background charge. Models of neutral defect complexes with the lowest formation energies were selected from Section 8.2 used in NEBs.

To fit the moment tensor potentials (MTPs), the training sets were generated with *ab initio* molecular dynamics (AIMD) simulations on $2 \times 2 \times 2$ supercells (256 atoms) of Li_3MO_4, which are geometrically optimized by DFT using the r^{2}SCAN functional. An NVT ensemble based on the Nosé−Hoover thermostat, and a time step of 0.5 fs were applied in the AIMDs.[73] A plane wave energy cutoff of the AIMDs was 400 eV. The total energy was integrated at the Γ point.[74]

For Li_3NbO_4 AIMDs, we performed simulations at 600, 800, 1000, and 1200 K, each lasting 8 ps for the equilibration step, and after a temperature ramping of 0.5 ps. In total, 8000 snapshots of the last 1 ps were taken as the training sets.[74] While for Li_3TaO_4, the temperature range was 600−1500 K with a step of 300 K. We investigate the role of defects on Li diffusion in Li_3MO_4 by considering two types of defects, i.e., the Li vacancy (Vac_{Li}) and the defect complex ($4Vac_{Li} + Nb_{Li}$ (Ta_{Li})). In the model of Li vacancy, a Li vacancy was introduced into a supercell of 256 atoms (a concentration of ~1%) and compensated with a background charge. We replaced one Li atom with an Nb (Ta) atom for complex antisite-vacancy defects and created four Li vacancies based on the most stable models calculated from Section 8.2, with concentrations of antisites of ~1% and Li vacancies of ~4%.

In training the MTPs, we chose the radius cutoff of 5 Å, and a maximum level of 12 controlling the completeness of basis functions during the training of the bulk structures and the defective structures with 0.5, 1, and 2% Li vacancies.[74,75] For structures with 4% Li vacancies or with the antisite defect complex, we increased R_{cut} to 6 Å to better capture the structural complexity of this situation. Weights on energies, forces, and stresses were set to 100:10:1. The accuracy of the MTP fittings is reported in Table S12.

MTP molecular dynamics (MTP-MD) simulations were conducted in LAMMPS[76] using the NVT ensemble (Nosé−Hoover).[73] We carried out long MDs of Li_3MO_4 for 10 ns with a time step of 1 fs, preceded by a temperature ramping of 10 ps, followed by 1 ns of equilibration. MDs used $4 \times 4 \times 4$ supercells with 2048 atoms. By varying the number of removed Li atoms, we computed the Li-ion conductivity of Li_3MO_4 structures including Vac_{Li} concentrations of 0.5, 1, 2, and 4%. By monitoring the mean-square displacements (see Figure S14) of Li^+ in MTP-MDs, we extracted the tracer diffusivity of eq 3

$$D^*(T) = \lim_{t\to\infty} \frac{1}{2dt}\left(\frac{1}{N}\sum_{i=1}^{N}\langle[\vec{r}_i(t) - \vec{r}_i(0)]^2\rangle\right) \quad (3)$$

where $d = 3$, N is the number of lithium ions, $\vec{r}_i(t)$ is the displacement of ith Li at time t. The activation energy of Li-ion migration (E_a) was derived from the Arrhenius equation

$$D^*(T) = D_0 \exp\left(-\frac{E_a}{k_B T}\right) \quad (4)$$

where D_0 is the prefactor, T is the temperature, and k_B is the Boltzmann constant. Li-ion conductivities $\sigma(T)$ are extracted from the Nernst−Einstein equation

$$\sigma(T) = \frac{nz^2e^2}{k_B T} D^*(T) \quad (5)$$

where n is the volume density of the Li^+, $z = +1$, and e is the electron charge.

■ ASSOCIATED CONTENT

Supporting Information

The Supporting Information is available free of charge at https://pubs.acs.org/doi/10.1021/acs.chemmater.3c01197.

(i) Synthesis and applications of lithium niobate and tantalate coating materials; (ii) structures of lithium niobate and tantalate compounds; (iii) analysis of intrinsic defects in lithium niobate and tantalate compounds; (iv) Li-ion migration barriers and migration paths vs. niobate or tantalate local environments; and (v) migration barriers extracted from moment tensor potential molecular dynamics (PDF)

■ AUTHOR INFORMATION

Corresponding Author

Pieremanuele Canepa − *Department of Materials Science and Engineering, National University of Singapore, 117575, Singapore; Department of Chemical and Biomolecular Engineering, National University of Singapore, 117585, Singapore;* orcid.org/0000-0002-5168-9253; Email: pcanepa@nus.edu.sg

https://doi.org/10.1021/acs.chemmater.3c01197
Chem. Mater. XXXX, XXX, XXX−XXX

Authors

Hengning Chen − *Department of Materials Science and Engineering, National University of Singapore, 117575, Singapore;* orcid.org/0009-0000-2475-4681

Zeyu Deng − *Department of Materials Science and Engineering, National University of Singapore, 117575, Singapore;* orcid.org/0000-0003-0109-9367

Yuheng Li − *Department of Materials Science and Engineering, National University of Singapore, 117575, Singapore;* orcid.org/0000-0002-1865-1122

Complete contact information is available at: https://pubs.acs.org/10.1021/acs.chemmater.3c01197

Notes

The authors declare no competing financial interest.

■ ACKNOWLEDGMENTS

P.C. acknowledges funding from the National Research Foundation under its NRF Fellowship NRFF12-2020-0012. The computational work was performed on resources of the National Supercomputing Centre, Singapore (https://www.nscc.sg).

■ REFERENCES

(1) Li, L.; Duan, H.; Li, J.; Zhang, L.; Deng, Y.; Chen, G. Toward High Performance All-Solid-State Lithium Batteries with High-Voltage Cathode Materials: Design Strategies for Solid Electrolytes, Cathode Interfaces, and Composite Electrodes. *Adv. Energy Mater.* **2021**, *11*, No. 2003154.

(2) Wang, K. X.; Li, X. H.; Chen, J. S. Surface and Interface Engineering of Electrode Materials for Lithium-Ion Batteries. *Adv. Mater.* **2015**, *27*, 527−545.

(3) Zhang, W.; Schröder, D.; Arlt, T.; Manke, I.; Koerver, R.; Pinedo, R.; Weber, D. A.; Sann, J.; Zeier, W. G.; Janek, J. (Electro)chemical expansion during cycling: monitoring the pressure changes in operating solid-state lithium batteries. *J. Mater. Chem. A* **2017**, *5*, 9929−9936.

(4) Famprikis, T.; Canepa, P.; Dawson, J. A.; Saiful Islam, M.; Masquelier, C. Fundamentals of inorganic solid-state electrolytes for batteries. *Nat. Mater.* **2019**, *18*, 1278−1291.

(5) Tan, D. H. S.; Wu, E. A.; Nguyen, H.; Chen, Z.; Marple, M. A. T.; Doux, J.-M.; Wang, X.; Yang, H.; Banerjee, A.; Meng, Y. S. Elucidating Reversible Electrochemical Redox of Li_6PS_5Cl Solid Electrolyte. *ACS Energy Lett.* **2019**, *4*, 2418−2427.

(6) Zhu, Y.; He, X.; Mo, Y. Origin of Outstanding Stability in the Lithium Solid Electrolyte Materials: Insights from Thermodynamic Analyses Based on First-Principles Calculations. *ACS Appl. Mater. Interfaces* **2015**, *7*, 23685−23693.

(7) Minnmann, P.; Strauss, F.; Bielefeld, A.; Ruess, R.; Adelhelm, P.; Burkhardt, S.; Dreyer, S. L.; Trevisanello, E.; Ehrenberg, H.; Brezesinski, T.; Richter, F. H.; Janek, J. Designing Cathodes and Cathode Active Materials for Solid-State Batteries. *Adv. Energy Mater.* **2022**, *12*, No. 2201425.

(8) Chen, Z.; Qin, Y.; Amine, K.; Sun, Y.-K. Role of surface coating on cathode materials for lithium-ion batteries. *J. Mater. Chem.* **2010**, *20*, 7606−7612.

(9) Culver, S. P.; Koerver, R.; Zeier, W. G.; Janek, J. On the Functionality of Coatings for Cathode Active Materials in Thiophosphate-Based All-Solid-State Batteries. *Adv. Energy Mater.* **2019**, *9*, No. 1900626.

(10) Ohta, N.; Takada, K.; Sakaguchi, I.; Zhang, L.; Ma, R.; Fukuda, K.; Osada, M.; Sasaki, T. $LiNbO_3$-coated $LiCoO_2$ as cathode material for all solid-state lithium secondary batteries. *Electrochem. Commun.* **2007**, *9*, 1486−1490.

(11) Peng, L.; Ren, H.; Zhang, J.; Chen, S.; Yu, C.; Miao, X.; Zhang, Z.; He, Z.; Yu, M.; Zhang, L.; Cheng, S.; Xie, J. $LiNbO_3$-coated $LiNi_{0.7}Co_{0.1}Mn_{0.2}O_2$ and chlorine-rich argyrodite enabling high-performance solid-state batteries under different temperatures. *Energy Storage Mater.* **2021**, *43*, 53−61.

(12) Liu, G.; Lu, Y.; Wan, H.; Weng, W.; Cai, L.; Li, Z.; Que, X.; Liu, H.; Yao, X. Passivation of the Cathode-Electrolyte Interface for 5 V-Class All-Solid-State Batteries. *ACS Appl. Mater. Interfaces* **2020**, *12*, 28083−28090.

(13) Heitjans, P.; Masoud, M.; Feldhoff, A.; Wilkening, M. NMR and impedance studies of nanocrystalline and amorphous ion conductors: lithium niobate as a model system. *Faraday Discuss.* **2007**, *134*, 67−82.

(14) Wilkening, M.; Epp, V.; Feldhoff, A.; Heitjans, P. Tuning the Li Diffusivity of Poor Ionic Conductors by Mechanical Treatment: High Li Conductivity of Strongly Defective $LiTaO_3$ Nanoparticles. *J. Phys. Chem. C* **2008**, *112*, 9291−9300.

(15) Zhang, Y.; Zhou, E.; Song, D.; Shi, X.; Wang, X.; Guo, J.; Zhang, L. Effects on electrochemical performances for host material caused by structure change of modifying material. *Phys. Chem. Chem. Phys.* **2014**, *16*, 17792−17798.

(16) Lu, G.; Peng, W.; Zhang, Y.; Wang, X.; Shi, X.; Song, D.; Zhang, H.; Zhang, L. Study on the formation, development and coating mechanism of new phases on interface in $LiNbO_3$-coated $LiCoO_2$. *Electrochim. Acta* **2021**, *368*, No. 137639.

(17) Xin, F.; Zhou, H.; Zong, Y.; Zuba, M.; Chen, Y.; Chernova, N. A.; Bai, J.; Pei, B.; Goel, A.; Rana, J.; Wang, F.; An, K.; Piper, L. F. J.; Zhou, G.; Whittingham, M. S. What is the Role of Nb in Nickel-Rich Layered Oxide Cathodes for Lithium-Ion Batteries? *ACS Energy Lett.* **2021**, *6*, 1377−1382.

(18) Lee, J. S.; Park, Y. J. Comparison of $LiTaO_3$ and $LiNbO_3$ Surface Layers Prepared by Post- And Precursor-Based Coating Methods for Ni-Rich Cathodes of All-Solid-State Batteries. *ACS Appl. Mater. Interfaces* **2021**, *13*, 38333−38345.

(19) Glass, A. M.; Nassau, K.; Negran, T. J. Ionic conductivity of quenched alkali niobate and tantalate glasses. *J. Appl. Phys.* **1978**, *49*, 4808−4811.

(20) Kim, J. H.; Kim, H.; Choi, W.; Park, M.-S. Bifunctional Surface Coating of $LiNbO_3$ on High-Ni Layered Cathode Materials for Lithium-Ion Batteries. *ACS Appl. Mater. Interfaces* **2020**, *12*, 35098−35104.

(21) Lee, H. B.; Hoang, T. D.; Byeon, Y. S.; Jung, H.; Moon, J.; Park, M.-S. Surface Stabilization of Ni-Rich Layered Cathode Materials via Surface Engineering with $LiTaO_3$ for Lithium-Ion Batteries. *ACS Appl. Mater. Interfaces* **2022**, *14*, 2731−2741.

(22) Iyi, N.; Kitamura, K.; Izumi, F.; Yamamoto, J. K.; Hayashi, T.; Asano, H.; Kimura, S. Comparative Study of Defect Structures in Lithium Niobate with Different Compositions. *J. Solid State Chem.* **1992**, *101*, 340−343.

(23) Smyth, D. M. Defects and transport in $LiNbO_3$. *Ferroelectrics* **1983**, *50*, 93−102.

(24) Kolb, E. D.; Laudise, R. A. The phase diagram, LiOH-Ta_2O_5-H_2O and the hydrothermal synthesis of $LiTaO_3$ and $LiNbO_3$. *J. Cryst. Growth* **1976**, *33*, 145−149.

(25) Bernasconi, P.; Montemezzani, G.; Günter, P.; Furukawa, Y.; Kitamura, K. Stoichiometric $LiTaO_3$ for ultraviolet photorefraction. *Ferroelectrics* **1999**, *223*, 373−379.

(26) Rahn, J.; Hüger, E.; Dörrer, L.; Ruprecht, B.; Heitjans, P.; Schmidt, H. Li self-diffusion in lithium niobate single crystals at low temperatures. *Phys. Chem. Chem. Phys.* **2012**, *14*, 2427−2433.

(27) Hüger, E.; Rahn, J.; Stahn, J.; Geue, T.; Heitjans Cd, P.; Schmidt, H. Lithium diffusion in congruent $LiNbO_3$ single crystals at low temperatures probed by neutron reflectometry. *Phys. Chem. Chem. Phys.* **2014**, *16*, 3670.

(28) Xin, F.; Zhou, H.; Bai, J.; Wang, F.; Whittingham, M. S. Conditioning the Surface and Bulk of High-Nickel Cathodes with a Nb Coating: An In Situ X-ray Study. *J. Phys. Chem. Lett.* **2021**, *12*, 7908−7913.

(29) Liao, Y.; Singh, P.; Li, W.; Goodenough, J. B. Comparison of Li^+ conductivity in $Li_{3-x}Nb_{1-x}M_xO_4$ (M = W, Mo) with that in $Li_{3-2x}Ni_xNbO_4$. *Mater. Res. Bull.* **2013**, *48*, 1372−1375.

(30) Yabuuchi, N.; Takeuchi, M.; Nakayama, M.; Shiiba, H.; Ogawa, M.; Nakayama, K.; Ohta, T.; Endo, D.; Ozaki, T.; Inamasu, T.; Sato, K.;

Komaba, S. High-capacity electrode materials for rechargeable lithium batteries: Li_3NbO_4-based system with cation-disordered rocksalt structure. *Proc. Natl. Acad. Sci. U.S.A.* **2015**, *112*, 7650−7655.
(31) Adams, S. From bond valence maps to energy landscapes for mobile ions in ion-conducting solids. *Solid State Ionics* **2006**, *177*, 1625−1630.
(32) Abrahams, S. C.; Reddy, J. M.; Bernstein, J. L. Ferroelectric lithium niobate 3. Single crystal X-ray diffraction study at 24°C. *J. Phys. Chem. Solids* **1966**, *27*, 997−1012.
(33) Volk, T.; Wöhlecke, M. *Lithium Niobate: Defects, Photorefraction and Ferroelectric Switching*; Springer Series in Materials Science; Springer: Berlin, 2008; Vol. *115*, p 4.
(34) Nyman, M.; Anderson, T. M.; Provencio, P. P. Comparison of Aqueous and Non-aqueous Soft-Chemical Syntheses of Lithium Niobate and Lithium Tantalate Powders. *Cryst. Growth Des.* **2009**, *9*, 1036−1040.
(35) Grenier, J.-C.; Martin, C.; Durif-Varambon, A. Étude cristallographique des orthoniobates et orthotantalates de lithium. *Bull. Mineral.* **1964**, *87*, 316−320.
(36) Hsiao, Y.-J.; Fang, T.-H.; Lin, S.-J.; Shieh, J.-M.; Ji, L.-W. Preparation and luminescent characteristic of Li_3NbO_4 nanophosphor. *J. Lumin.* **2010**, *130*, 1863−1865.
(37) Modeshia, D. R.; Walton, R. I.; Mitchell, M. R.; E Ashbrook, S. Disordered lithium niobate rock-salt materials prepared by hydrothermal synthesis. *Dalton Trans.* **2010**, *39*, 6021−6036.
(38) Mather, G. C.; Dussarrat, C.; Etourneau, J.; West, A. R. A review of cation-ordered rock salt superstructure oxides. *J. Mater. Chem.* **2000**, *10*, 2219−2230.
(39) Zocchi, M.; Gatt1, M.; Santoro, A.; Roth, R. S. Neutron and X-Ray Diffraction Study on Polymorphism in Lithium Orthotantalate, Li_3TaO_4. *J. Solid State Chem.* **1983**, *48*, 420−430.
(40) Du Boulay, D.; Sakaguchi, A.; Suda, K.; Ishizawa, N. Reinvestigation β-Li_3TaO_4. *Acta Crystallogr., Sect. E: Struct. Rep. Online* **2003**, *59*, i80−i82.
(41) Kim, C.; Pham, T. L.; Lee, J.-S.; Kim, Y.-I. Synthesis, thermal analysis, and band gap of ordered and disordered complex rock salt Li_3TaO_4. *J. Solid State Chem.* **2022**, *315*, 123450.
(42) Allemann, J.; Xia, Y.; Morriss, R. E.; Wilkinson, A. P.; Eckert, H.; Speck, J.; Levi, C. G.; Lange, F. F.; Anderson, S. Crystallization behavior of $Li_{1-5x}Ta_{1+x}O_3$ glasses synthesized from liquid precursors. *J. Mater. Res.* **1996**, *11*, 2376−2387.
(43) Xiao, Y.; Miara, L. J.; Wang, Y.; Ceder, G. Computational Screening of Cathode Coatings for Solid-State Batteries. *Joule* **2019**, *3*, 1252−1275.
(44) Zhu, Y.; He, X.; Mo, Y. First principles study on electrochemical and chemical stability of solid electrolyte-electrode interfaces in all-solid-state Li-ion batteries. *J. Mater. Chem. A* **2016**, *4*, 3253.
(45) Scott, B. A.; Burns, G. Determination of Stoichiometry Variations in $LiNbO_3$ and $LiTaO_3$ by Raman Powder Spectroscopy. *J. Am. Ceram. Soc.* **1972**, *55*, 225−230.
(46) Lerner, P.; Legras, C.; Dumas, J. P. Stoichiometry of lithium metaniobate single crystals. *J. Cryst. Growth* **1968**, *3*, 231−235.
(47) Wilkinson, A. P.; Cheetham, A. K.; Jarman, R. H. The defect structure of congruently melting lithium niobate. *J. Appl. Phys.* **1993**, *74*, 3080−3083.
(48) Blümel, J.; Born, E.; Metzger, T. Solid state NMR study supporting the lithium vacancy defect model in congruent lithium niobate. *J. Phys. Chem. Solids* **1994**, *55*, 589−593.
(49) Xu, H.; Lee, D.; He, J.; Sinnott, S. B.; Gopalan, V.; Dierolf, V.; Phillpot, S. R. Stability of intrinsic defects and defect clusters in $LiNbO_3$ from density functional theory calculations. *Phys. Rev. B* **2008**, *78*, No. 174103.
(50) Donnerberg, H.; Tomlinson, S. M.; Catlow, C. R. A.; Schirmer, O. F. Computer-simulation studies of intrinsic defects in $LiNbO_3$ crystals. *Phys. Rev. B* **1989**, *40*, 11909−11916.
(51) Kuganathan, N.; Kordatos, A.; Kelaidis, N.; Chroneos, A. Defects, Lithium Mobility and Tetravalent Dopants in the Li_3NbO_4 Cathode Material. *Sci. Rep.* **2019**, *9*, No. 2192.
(52) Canepa, P.; Gopalakrishnan, S.; Gautam; Broberg, D.; Bo, S.-H.; Ceder, G. Role of Point Defects in Spinel Mg Chalcogenide Conductors. *Chem. Mater.* **2017**, *29*, 9657−9667.
(53) Li, Y.; Canepa, P.; Gorai, P. Role of Electronic Passivation in Stabilizing the Lithium-$Li_xPO_yN_z$ Solid-Electrolyte Interphase. *PRX Energy* **2022**, *1*, No. 023004.
(54) Li, Y.; Schmidt, W. G.; Sanna, S. Defect complexes in congruent $LiNbO_3$ and their optical signatures. *Phys. Rev. B* **2015**, *91*, No. 174106.
(55) Gubaev, K.; Podryabinkin, E. V.; Hart, G. L. W.; Shapeev, A. V. Accelerating high-throughput searches for new alloys with active learning of interatomic potentials. *Comput. Mater. Sci.* **2019**, *156*, 148−156.
(56) Ruprecht, B.; Heitjans, P. Ultraslow lithium diffusion in Li_3NbO_4 probed by 7Li simulated Echo NMR Spectroscopy. *Diffus. Fundam.* **2010**, *12*, 100−101.
(57) Kim, C.; Kim, Y.-I. Ionic Conductivity of Li_3TaO_4 Depending on Polymorphism and Non-Stoichiometric Defects. *Ceram. Int.* **2023**, No. 212.
(58) Xin, F.; Goel, A.; Chen, X.; Zhou, H.; Bai, J.; Liu, S.; Wang, F.; Zhou, G.; Whittingham, M. S. Electrochemical Characterization and Microstructure Evolution of Ni-Rich Layered Cathode Materials by Niobium Coating/Substitution. *Chem. Mater.* **2022**, *34*, 7858−7866.
(59) Chen, T.; Sai Gautam, G.; Canepa, P. Ionic Transport in Potential Coating Materials for Mg Batteries. *Chem. Mater.* **2019**, *31*, 8087−8099.
(60) Gorai, P.; Famprikis, T.; Singh, B.; Stevanović, V.; Canepa, P. Devil is in the Defects: Electronic Conductivity in Solid Electrolytes. *Chem. Mater.* **2021**, *33*, 7484−7498.
(61) Kresse, G.; Furthmü, J. Efficient iterative schemes for ab initio total-energy calculations using a plane-wave basis set. *Phys. Rev. B* **1996**, *54*, 11169−11186.
(62) Kresse, G.; Joubert, D. From ultrasoft pseudopotentials to the projector augmented-wave method. *Phys. Rev. B* **1999**, *59*, 1758−1775.
(63) Furness, J. W.; Kaplan, A. D.; Ning, J.; Perdew, J. P.; Sun, J. Accurate and Numerically Efficient r^2SCAN Meta-Generalized Gradient Approximation. *J. Phys. Chem. Lett.* **2020**, *11*, 8208−8215.
(64) Perdew, J. P.; Burke, K.; Ernzerhof, M. Generalized Gradient Approximation Made Simple. *Phys. Rev. Lett.* **1996**, *77*, 3865−3868.
(65) Ong, S. P.; Davidson Richards, W.; Jain, A.; Hautier, G.; Kocher, M.; Cholia, S.; Gunter, D.; Chevrier, V. L.; Persson, K. A.; Ceder, G. Python Materials Genomics (pymatgen): A robust, open-source python library for materials analysis. *Comput. Mater. Sci.* **2013**, *68*, 314−319.
(66) Zhang, Z. G.; Abe, T.; Moriyoshi, C.; Tanaka, H.; Kuroiwa, Y. Study of materials structure physics of isomorphic $LiNbO_3$ and $LiTaO_3$ ferroelectrics by synchrotron radiation X-ray diffraction. *Jpn. J. Appl. Phys.* **2018**, *57*, No. 11UB04.
(67) Hsu, R.; Maslen, E. N.; du Boulay, D.; Ishizawa, N. Synchrotron X-ray Studies of $LiNbO_3$ and $LiTaO_3$. *Acta Crystallogr., Sect. B: Struct. Sci.* **1997**, *53*, 420−428.
(68) Jacquet, Q.; Perez, A.; Batuk, D.; Tendeloo, G. V.; Rousse, G.; Tarascon, J.-M. The $Li_3Ru_yNb_{1-y}O_4$ ($0 \le y \le 1$) System: Structural Diversity and Li Insertion and Extraction Capabilities. *Chem. Mater.* **2017**, *29*, 5331−5343.
(69) Freysoldt, C.; Neugebauer, J.; Van De Walle, C. G. Fully Ab Initio Finite-Size Corrections for Charged-Defect Supercell Calculations. *Phys. Rev. Lett.* **2009**, *102*, No. 016402.
(70) Kumagai, Y.; Oba, F. Electrostatics-based finite-size corrections for first-principles point defect calculations. *Phys. Rev. B* **2014**, *89*, No. 195205.
(71) Adams, S. Relationship between bond valence and bond softness of alkali halides and chalcogenides. *Acta Crystallogr., Sect. B: Struct. Sci.* **2001**, *57*, 278−287.
(72) Sheppard, D.; Terrell, R.; Henkelman, G. Optimization methods for finding minimum energy paths. *J. Chem. Phys.* **2008**, *128*, No. 94107.
(73) Hoover, W. G. Canonical dynamics: Equilibrium phase-space distributions. *Phys. Rev. A* **1985**, *31*, 1695−1697.
(74) Wang, J.; Panchal, A. A.; Pieremanuele, C. Strategies for fitting accurate machine-learned inter-atomic potentials for solid electrolytes

https://doi.org/10.1021/acs.chemmater.3c01197
Chem. Mater. XXXX, XXX, XXX−XXX

machine-learned inter-atomic potentials for solid electrolytes. *Mater. Futures* **2023**, *2*, No. 015101.
(75) Zuo, Y.; Chen, C.; Li, X.; Deng, Z.; Chen, Y.; Behler, J.; Csányi, G.; Shapeev, A. V.; Thompson, A. P.; Wood, M. A.; Ong, S. P. Performance and Cost Assessment of Machine Learning Interatomic Potentials. *J. Phys. Chem. A* **2020**, *124*, 731−745.
(76) Plimpton, S. Fast Parallel Algorithms for Short-Range Molecular Dynamics. *J. Comput. Phys.* **1995**, *117*, 1−13.

https://doi.org/10.1021/acs.chemmater.3c01197
Chem. Mater. XXXX, XXX, XXX−XXX